Multiscale modeling of rock fracture in comminution — A comparative study of FEM accuracy and DEM scalability

Minerals Engineering 232 (2025) 109488

Contents lists available at ScienceDirect

Minerals Engineering

journal homepage: www.elsevier.com/locate/mineng

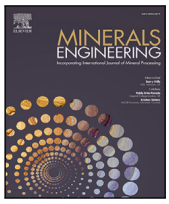

Multiscale modeling of rock fracture in comminution — A comparative study of FEM accuracy and DEM scalability

Laura Suarez [a,1], Vedad Tojaga [b,1], Erik Olsson [a,*], Adam Bilock [c], Magnus Evertsson [d], Jörgen Kajberg [a], Johannes Quist [b,d,*]

[a] Division of Solid Mechanics, Luleå, University of Technology, Luleå, Sweden
[b] Department of Computational Engineering and Design, Fraunhofer-Chalmers Centre for Industrial Mathematics, Gothenburg, Sweden
[c] IPS Particle Technology AB, Gothenburg, Sweden
[d] Department of Industrial and Materials Science, Chalmers University of Technology, Gothenburg, Sweden

ARTICLE INFO

Keywords:
DEM
Bonded particle model
FEM
Quasi-brittle fracture
Crushing
Comminution

ABSTRACT

The growing global demand for minerals and metals, coupled with the need for improved energy and water efficiency in resource extraction, has led to the use of numerical modeling, particularly the discrete element method (DEM), to evaluate and optimize comminution processes that account for a significant portion of the energy consumption in mineral and metal extraction. Despite advancements, a significant challenge remains in balancing the local resolution of fractures at the rock particle level, where physics-based material models using the finite element method (FEM) have excelled, with the resolution of industrial-scale total particle interactions within the machine system. This work explores the high-resolution fracture of rock particles using an established material model implemented within FEM as a valuable reference for fractures with a balanced mid-level resolution achieved through a bonded discrete element method applicable to industrial-scale systems. Brazilian tests were performed on two rock types to calibrate the models. Single particle breakage (SPB) experiments employing digital image correlation (DIC) were conducted to evaluate the performance of the models. Finally, the DEM model was demonstrated in an industrial-scale cone crusher application. The results show good agreement for the highly resolved FEM approach (requiring only two material parameters to be determined, which is particularly advantageous for generating virtual particle breakage data across various rock materials, shapes, and sizes) and reasonable agreement for the DEM fracture response, which is attributed to the much coarser mesh used that does not capture the crumbling mechanism (as revealed by the comparison between the two numerical approaches). Despite these discrepancies, the cone crusher predictions fall within the expected ranges for the system response at the machine level.

1. Introduction

There is growing demand for metals and minerals to support the green transition of society. Comminution, which is the process of reducing the size of rocks, is essential for liberating valuable minerals. The mining sector is currently responsible for nearly 2% of the global total energy use but is likely to increase significantly by a factor of two to eight by 2060 (Aramendia et al., 2023). Nearly half of this energy is used in comminution processes, where the inefficient grinding processes of ore are the largest single-energy consumers (Jeswiet and Szekeres, 2016). To reduce energy consumption, new and optimized comminution equipment is essential. In this context, a virtual comminution development platform plays a key role in facilitating the development of energy-efficient rock processing solutions, considering the significant costs and time involved in physical testing. Additionally, simulation-based engineering evaluations enable the identification of the optimal operation of existing comminution devices, for instance depending on specific ore mineralogy and competence. The discrete element method (DEM), pioneered by Cundall and Strack (1979), is the preferred approach for modeling processes involving granular materials. However, the most challenging aspect of comminution modeling using DEM is that a mechanistic model is of limited use, without

* Corresponding authors.
E-mail addresses: laura.suarez@ltu.se (L. Suarez), vedad.tojaga@fcc.chalmers.se (V. Tojaga), erik.1.olsson@ltu.se (E. Olsson), adam.bilock@industrialpathsolutions.com (A. Bilock), magnus.evertsson@chalmers.se (M. Evertsson), jorgen.kajberg@ltu.se (J. Kajberg), johannes.quist@fcc.chalmers.se (J. Quist).
[1] These authors contributed equally to this work.

https://doi.org/10.1016/j.mineng.2025.109488
Received 7 April 2025; Received in revised form 30 May 2025; Accepted 1 June 2025
Available online 24 June 2025

the ability to mathematically describe the rock's response to applied forces (Weerasekara et al., 2013). The challenge lies in bridging the gap between the mesoscale behavior of individual rock particles and the macroscale operation of industrial comminution devices. A successful solution must accurately capture the relevant fracture physics at the single-particle level while enabling the simulation of large particle assemblies within an industrial-scale machine. This paper aims to address this critical problem.

In the rock mechanics and geomechanics research community, the focus is typically on a single rock specimen, often cylindrical or rectangular, with or without a predefined crack. Historically, from a modeler's perspective, rocks have been viewed as assemblies of glued particles, where each particle represents a grain, and the glue represents the cement holding the grains together, allowing for the modeling of inter-granular fracture (examples include the bonded discrete element method (Potapov and Campbell, 1994; Orozco et al., 2019; Cantor et al., 2017; Kun and Herrmann, 1996; Potyondy and Cundall, 2004) and the lattice element method (Zubelewicz and Bažant, 1987; Bažant et al., 1990; Ibrahimbegovic and Delaplace, 2003; Nikolić et al., 2018; Cusatis et al., 2011)) as well as intra-granular fracture (Wessling et al., 2022). The bonded particle model (BPM) by Potyondy and Cundall (2004) is perhaps the most well-known approach for treating rocks in this manner. In this model, spherical particles are connected by virtual Timoshenko beams. When the maximum tensile or shear stress within a beam exceeds its tensile or shear strength, the beam is removed, leaving a contact model between the now-disconnected particles. Alternatively, Voronoi cell tessellation may be used instead of spherical particles, as bonding them along their faces helps with volume preservation during the fragmentation process, among other benefits (Orozco et al., 2019; Cantor et al., 2017; Ibrahimbegovic and Delaplace, 2003). Additional advantages of using Voronoi cells as opposed to spheres include their closer resemblance to the irregular, polyhedral shapes of some types of natural mineral grains, their ability to achieve higher packing densities, and the ease with which varying grain sizes and heterogeneity can be incorporated into the bonded cell model. Furthermore, Voronoi cells generate more realistic and complex fracture patterns along grain boundaries or weak planes. High-resolution imaging and segmentation techniques such as X-ray computed tomography (CT) and digital image processing can be employed to accurately capture realistic grain shape distributions in large-scale samples. While Voronoi cells may introduce some computational overhead due to their intricate shapes, they can actually be more efficient by minimizing the need for excessively fine discretizations. The bonded particle model by Potyondy and Cundall has entered the field of comminution (Jiang et al., 2023; Quist and Evertsson, 2016) with a coarser mesh resolution because of its much larger scale compared with that of a single rock specimen (Khanal et al., 2005; Ergenzinger et al., 2011; Wessling et al., 2023). A good example of this application is the work performed by Quist and Evertsson (2016) in which compression tests were conducted, and the bonded particle model was calibrated against the size-dependent force required to break a rock for use in crushing simulations.

Instead of modeling rock fracture explicitly and to speed up the DEM simulation, once a failure criterion is met, the particle can be replaced with a collection of progeny fragments or new particles (not all rock fragments are considered throughout the entire simulation, as seen in the bonded particle model), commonly referred to as the particle replacement method (PRM), which is the most frequently applied approach in comminution modeling using DEM (Cleary, 2001; André and Tavares, 2020; Delaney et al., 2015; Denzel et al., 2023). While the parent particle is most often a sphere, various shapes are used for progeny particles, such as spheres or clumped spheres (Barrios et al., 2020; Brzeziński and Gladky, 2022; Cleary and Sinnott, 2015; Li et al., 2014; Tavares et al., 2021), superquadrics (Delaney et al., 2015), and polyhedral cells (de Arruda Tino and Tavares, 2022; Tavares et al., 2020). Traditionally, the failure criterion is based on the probability of fracture given the specific amount of energy required to break a rock. This criterion is determined using methods such as the drop-weight test, which has been enhanced with instrumentation for real-time measurements, or through compression tests (King and Bourgeois, 1993; Tavares, 2007; Tavares and King, 1998). If the energy absorbed by the particle during particle–particle or particle–plane contact meets the specific fracture energy criteria, it breaks or can undergo damage by reducing the fracture energy due to repeated low-energy impacts (Tavares and King, 2002). Each fragment is then allocated a new fracture energy corresponding to its size, and inherits the kinematics from the parent particle. The fragments inherit both the linear and angular velocities and, consequently, the kinetic energy of the parent particle, which affects the flow behavior on the conveying equipment. Overall, the particle replacement method does not capture the force–displacement response as accurately as the bonded particle model or as well as in rock mechanics where physics-based material models using the finite element method (FEM) have excelled, nor can it accurately predict rock fragmentation. However, its key strength lies in its ability to be conveniently calibrated against the product size distribution (Jiménez-Herrera et al., 2018). The PRM approach has been proven to be effective in comminution devices dominated by impact-breakage failure modes, whereas machines dominated by compressive breakage are more challenging. Additionally, challenges arise related to the conservation of mass and momentum due to the replacement and introduction of new particles or elements within the same confined spatial domain previously occupied by the parent particle.

However, to the best of the authors' knowledge, no published studies have performed a one-to-one shape correspondence between models and experiments involving irregular rock particles, despite the critical role that the particle shape plays in the computational modeling of granular materials (Zhao et al., 2023; Kawamoto et al., 2016). Instead, it is more common to compare the distributions of fracture responses of irregular rock particles (Mwanga et al., 2015; Eliáš, 2014). That is, ensuring that the predicted force–displacement response of rock particles, as well as rock fragmentation in industrial-scale machine simulations involving large particle assemblies, aligns with that of actual rock remains a research gap; rather, the focus has predominantly been on reproducing the product size distribution.

1.1. Outline

The key novelty of this work lies in its attempt to bridge the gap between accurately capturing the rock material response at the single-particle level and simultaneously facilitating the simulation of an industrial cone crusher. The following main analyses are performed:

- Detailed modeling of the rock fracture using a FEM approach (Section 3) with a probabilistic fracture model and a detailed mesh to obtain high resolution of the fragmentation.
- A bonded discrete element model with Voronoi cells (Section 4) is used to model particle breakage at a lower resolution, sufficient to capture the overall response but not as detailed as the FEM model, while enabling full machine simulation.
- Both the FEM (Section 5.1) and DEM models (Section 5.2) are calibrated using the Brazilian indirect tensile strength test (Section 2.1).
- The fracture response and behavior are evaluated and validated using single-particle breakage compression tests with digital image correlation (DIC) (Section 2.2), with both the FEM (Section 6.1) and DEM approaches (Section 6.2).
- The breakage response from the high-resolution FEM and the lower-resolution DEM is compared and analyzed (Section 7).
- Finally, the utilization of the DEM model is demonstrated in an industrial-scale cone crusher case (Section 8).

2. Experiments

Indirect tensile tests were conducted to calibrate, and single particle breakage (SPB) tests were carried out to validate the fracture models presented in Sections 3 and 4. The following section describes briefly these testing methods and presents information about the material, specimen preparation and experimental setup.

2.1. Indirect tensile strength tests

Diametrical compression tests, also known as the Brazilian disc test (BDT) were performed. This is a bi-axial test that allows to determine the tensile strength of brittle material indirectly by loading a cylinder along its diameter to induce tensile stresses normal to the loading direction, which are constant over a region around the center. As a consequence, crack initiation occurs in a high tensile zone, theoretically, around the geometrical center of the specimen. Under the assumption of plane stress (Jonsén et al., 2007), the ultimate tensile strength (UTS) of the material can be estimated by Eq. (1) (Hondros, 1959).

$$UTS = \frac{2F}{\pi Dt} \tag{1}$$

Here, F is the force at failure, D the diameter, and t the thickness.

Cylindrical specimens of granite from Glimmingen and limestone from Falköping with flat ends were drilled and cut. It should be noted that aggregate rock type materials were used for the experiments, while the overall scope of the approach intends to also focus on the comminution of ore materials. In order to get access to both crushed rock particles, as well as high-quality drill core samples, the most practical approach was to sample both specimens for single particle tests, as well as larger slabs for drill core specimen extraction, from the same blasting charge. In this way, the mineralogical correspondence between the specimens is well controlled. Following the recommendations from the standard ASTM D3967-16 of having a diameter at least ten times larger than the largest grain size, a diameter of 44.8 mm and a thickness-to-diameter ratio $t/D \approx 0.3$ was selected. Quasi-static compression tests of BDT specimens (6 limestone and 10 granite specimens) were performed with an electro-mechanical loading machine (Dartec M1000/RE) with maximum capacity of 100 kN and a maximum stroke of 100 mm. The surfaces at the contact points were lubricated to reduce the friction effects. The load was monotonically increased by controlling the displacement to 0.2 mm/min and the force was measured continuously with a load cell with a maximum capacity of 22 kN and an accuracy of ±0.14%.

Digital image correlation (DIC) techniques to obtain full displacement and deformation fields on the surface of the specimens were implemented. 2D digital images of BDT specimens were taken at 2 frames per second (fps) with Aramis (V6.3.1) Digital Image Correlation System (GOM mbH, Germany) and processed with an integrated software to determine the evolution of strain fields. The specimens were prepared by sandblasting the surface and then spraying black and white Boron Nitride Aerosol paint on it to obtain non-directional, high contrast and stochastic pattern. An external axial extensometer (Model 3542-025M, Epsilon Corp) sampling at 100 Hz was used as a backup measuring system.

Displacements in the material were obtained for the calibration of FEM models via a virtual extensometer of $l = 20$ mm set along the loading direction around the geometrical center of the specimen to avoid non-linear deformations at the contact points due to Hertzian contact effects (see Fig. 1(a)). An external extensometer of length $\mathcal{L}$ was also used because of the coarser mesh resolution used in the DEM model.

2.2. Single irregular particle breakage test

Seven irregular granite rock pieces from Glimmingen quarry and seven limestone pieces from Falköping quarry, each of different sizes and shapes were obtained for testing. Single particle breakage tests on the rock pieces were performed using an Instron 400RD hydraulic machine (Max. capacity = 2000 kN) and a digital image correlation system (Zeiss ARAMIS) at 100 frames per second to obtain deformation fields on the surface (see Fig. 1(b)). The loading rate was set at 18 mm/min, and the data sampling rate was 1000 Hz. The 3D laser scanning of the rock particles was done using a ZEISS Scanbox 4105. To achieve a close correspondence in the positioning of the particles in the experimental setup and the simulation setup, the 3D models of the particles were first positioned in the virtual environment. Then, before each experiment, the specific particle was positioned in the compression device with as little deviation as possible from the virtual position of the corresponding 3D model. The resulting deviation in height between the loading plates in the simulation and the experimental position was below 0.68% on average, 0.34% median, and 1.95% maximum. Figs. 2(a) and 2(c) show the crack paths after the initial fracture event, identified by the first notable drop in force. The corresponding failure loads are listed in Table 6.

3. Finite element model

The numerical simulations of the experiments were performed in the multi-purpose finite element software ABAQUS (Dassault Systèmes Simulia Corp, 2022) using the explicit time integration method. More information about the material model and numerical setup is provided below.

3.1. FEM material model

The rock material shows a complicated constitutive behavior with non-linear elasticity, damage driven by shear in compression and by normal stresses in tension, and a strong strain rate sensitivity. An additional complexity is its heterogeneity on different scales. It is critical to describe the rock material behavior with an appropriate constitutive law capturing the relevant effects for the intended application. Shear driven damage in compression has successfully been modeled using a pressure dependent plasticity model (Krieg, 1978; Swenson and Taylor, 1983). This model coupled with a probabilistic model for tensile fracture (Denoual and Hild, 2000; François Hild and da Silva, 2003; Forquin and Hild, 2010) constitutes the KST-DFH model. The model provides an effective approach for predicting rock fracture in different applications like percussive drilling, ballistics, and contact loading. This model will be relied upon in this work as well. To capture the strain rate sensitivity, a viscoplastic modeling approach has been used successfully (Saksala, 2010; Saksala et al., 2013).

Initially, the material behavior is assumed to be elastic, and isotropic elasticity is characterized by the Young's modulus E and Poisson's ratio ν. Brittle materials can fracture in both compression due to shear failure and, naturally in tension. To predict both these types of damage in rocks with FEM, a simplified version of the well-proven KST-DFH constitutive model (named after the authors (Denoual and Hild, 2000; Forquin and Hild, 2010; Krieg, 1978; Swenson and Taylor, 1983)) was used, presently utilizing only the quasi-static description of the material behavior. The model describes the behavior of mineral materials under low and high confining pressures as well as damage due to tensile cracking initiating from random micro defects (Saadati et al., 2014; Olsson et al., 2019).

The KST part of the model describes the damage in compression under different confining pressures due to shear failure using a plasticity-like model. The yield surface, describing when shear failure occurs is given by

$$\sigma_{eq} = \sqrt{a_0{}^2 + a_1 P + a_2 P^2}. \tag{2}$$

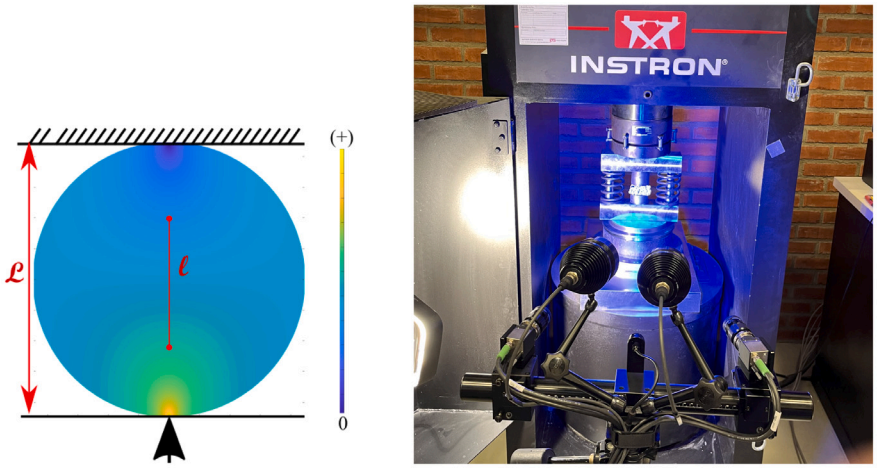

(a) (b)

Fig. 1. Figure (a) illustrates the Brazilian disc specimen and boundary conditions. Color contours display the analytical solution for the vertical displacements of a point load configuration. The red lines indicate the position of the virtual extensometer of length l used in the calibration of the FEM and external extensometer of length $\mathcal{L}$ used in DEM. Figure (b) present an image of the single particle breakage test setup. (For interpretation of the references to color in this figure legend, the reader is referred to the web version of this article.)

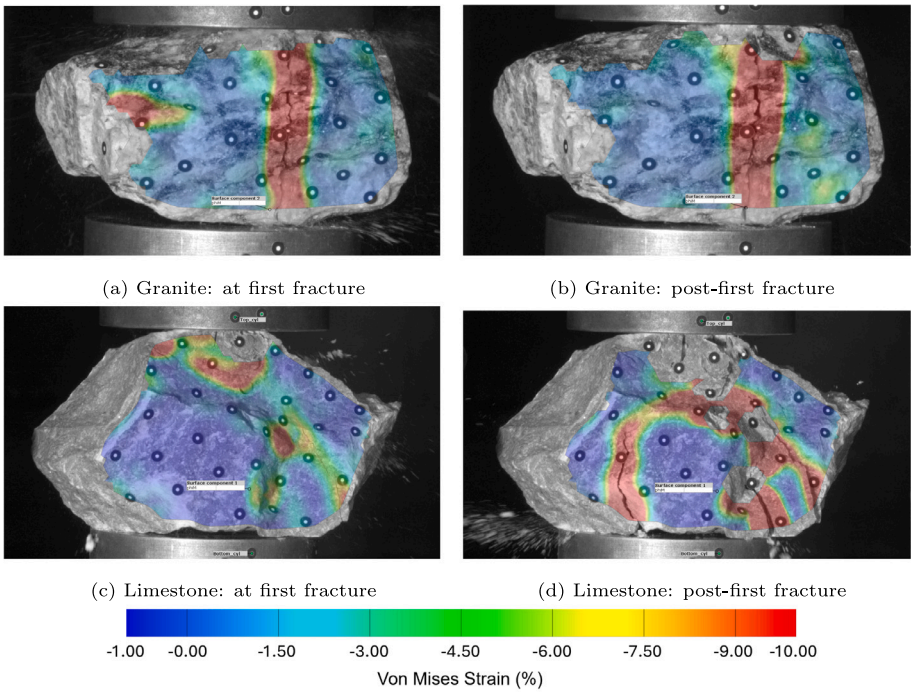

(a) Granite: at first fracture (b) Granite: post-first fracture

(c) Limestone: at first fracture (d) Limestone: post-first fracture

Fig. 2. Deformation in terms of von Mises strain fields of (a–b) granite and (c–d) limestone samples at first fracture, identified at first load drop, and post-first fracture. Crack patterns are identified as strain localization zones on the surface and visualized by warm colors, i.e., the red color represents a high strain, whereas the blue color represents a low strain. (For interpretation of the references to color in this figure legend, the reader is referred to the web version of this article.)

Here, a_0, a_1, a_2 are material parameters and P is the hydrostatic pressure. The yield surface is assumed to be constant regardless of plastic deformations. Furthermore, the KST model includes a piecewise linear function linking the volumetric strain $\varepsilon_v^{(n)}$ to the hydrostatic pressure $P^{(n)}$ due to the collapse of pores (where $n = 1, 2...N$ stages of inelastic compaction). However, this effect was small in the present study, because the studied materials contained only a small fraction of pores (Saadati et al., 2018).

Damage due to tensile cracking is handled by the DFH part of the model, which represents an anisotropic damage formulation. This model describes the probabilistic behavior of brittle materials accounting for crack initiation at the weakest defect in a considered volume. The model provides the tensile failure stress in a principal stress direction i for an element in the model, $\sigma_F^{(i)}$ by

$$P_F = 1 - \exp\left[-\left(\frac{\sigma_F^{(i)}}{\sigma_0}\right)^m \frac{V_{el}}{V_{ref}}\right], \tag{3}$$

where P_F is the probability of failure, σ_0 is the Weibull scale parameter, m the Weibull exponent, V_{el} the element volume associated with the studied integration point, and V_{ref} an arbitrary reference volume introduced for dimensional consistency. A consequence of this material description is that larger elements will have a lower average failure stress as the probability of finding critical defects is larger in larger elements. The average failure stress σ_w of a volume V_{ref} is specified as

a material parameter given by Eq. (4), making a smooth transition from uniaxial tensile testing to the finite element model and the consequence is that a tensile sample with volume V_{ref} will have an average tensile strength of σ_w,

$$\sigma_w = \sigma_0 \Gamma\left(1 + \frac{1}{m}\right) \tag{4}$$

where $\Gamma(x)$ is the gamma function. Damage occurs when the principal stress in direction (i) exceeds the critical stress in that direction, $\sigma_F^{(i)}$, randomly sampled for each element using the probability distribution given in Eq. (3). A consequence of the anisotropic damage model is that if the material has failed in one principal direction, it still has a tensile strength in the other two perpendicular principal direction, mimicking the behavior of a crack. The benefit of using the DFH model is two-fold; scatter in experimental data can be due to the probabilistic description of the failure stress and a statistical volume effect can also be captured as larger loaded volumes have a higher probability of containing defects of a given critical size.

Previous studies (Erzar and Forquin, 2014; Saadati et al., 2016) have shown that the activation, growth, and propagation of cracks occur along with a bridging phenomenon that locally resists crack opening, resulting in softening behavior under dynamic tension. When the material is exposed to high tensile stress rates, cracks nucleate when the tensile stress reaches a critical value and propagate until they encounter other defects that have also formed in front of them, resulting in relaxation effects around the crack tip (Denoual and Hild, 2000). This phenomena can be included in the model as an extra cohesive stress term σ_{coh} added to the macroscopic principal stress Σ_i. However, this cohesive behavior is set to zero in the present work as this effect has mainly been seen under dynamic load conditions and thus complete failure of the material in direction (i) occurs if the critical stress is exceeded. More details on how the anisotropic damage model works can be found for instance in Olsson et al. (2019).

4. Discrete element model

In DEM (Cundall and Strack, 1979), each particle interacts with neighboring particles through contact forces, and its motion is governed by Newton's second law. The ordinary differential equations (ODEs) can be solved using explicit time integration methods such as forward Euler and the velocity Verlet algorithm (Cundall and Strack, 1979; Govender et al., 2014; Rozmanov and Kusalik, 2010). To update the positions and orientations of the particles at each time step, the Verlet velocity algorithm was used for the translation and forward Euler, for the rotational integration. The particles are pseudo-rigid, meaning they can overlap, provided the overlap distance is small compared to the particle size, such that the deformation of the particles is negligible. This assumption requires small time steps to achieve slight overlaps and maintain numerical stability. Explicit methods, particularly with parallel computing, offer efficient and scalable solutions for industrial-sized problems involving large-particle systems. The in-house software Demify, developed at the Fraunhofer-Chalmers Centre, leveraging High-Performance Computing (HPC) on Graphical Processing Units (GPUs) was utilized to achieve these capabilities.

The bonded particle model (BPM) (Potyondy and Cundall, 2004) is a variation of DEM that introduces virtual, yet removable, cohesive bonds in the form of Timoshenko beams between spherical particles, mimicking the natural bonds (cement) found between grains in rock, thereby simulating rock fracture. Since the inception of spherical BPM, a number of extensions have emerged, including polyhedral block BPM (Liu et al., 2020). In contrast, the particles were treated as Voronoi cells bonded at the nodes, preserving both mass and volume during the breakage process, similar to the bonded cell model (Potapov and Campbell, 1994; Cantor et al., 2017; Orozco et al., 2019; Kun and Herrmann, 1996; Asahina and Bolander, 2011). This approach also reduces the number of elements required to capture nontrivial shapes compared to spheres. For example, in Fig. 3(a), 50 Voronoi cells were used to discretize the rock, which differs from many other DEM computer codes that use spherical particles. Additionally, the constitutive response of the bonds was defined using a traction–separation description (Liu and Ji, 2019; Ma et al., 2014; Li et al., 2024; Ma et al., 2016). This method is in contrast to the sudden load drop and mesh-dependent energy dissipation observed in the BPM, as it maintains a fixed area under the traction–separation law across mesh sizes (Wang et al., 2023). The chosen approach resembles the lattice element model utilizing the strong discontinuity approach but includes element overlap (Nikolić et al., 2018).

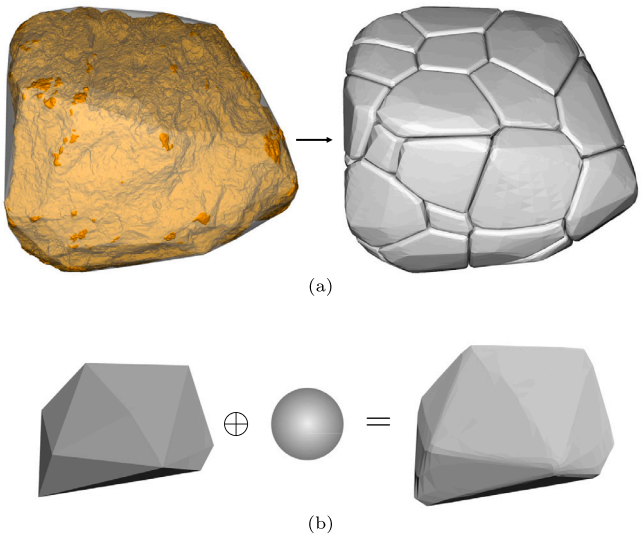

Fig. 3. (a) Bonded Voronoi-particle model generated from the approximation of the scanned (golden) rock surface using the convex hull method. (b) The dilated polyhedron is the union of a sphere and a polyhedron (illustration courtesy of Anita Ullrich). (For interpretation of the references to color in this figure legend, the reader is referred to the web version of this article.)

In Demify, points inside the spatial domains were randomly placed, including the Brazilian discs and scanned rocks, with a minimum allowed distance, referred to as the pruning distance. The Voro++ library (Rycroft, 2009) was used to compute the Voronoi tesselations of the spatial domain and the randomly sampled points. A convex surface was generated for the non-convex scanned rocks using the convex hull method in MeshLab, which is an open-source system for processing and editing 3D triangular meshes, as depicted in Fig. 3(a). Each Voronoi cell was treated as a dilated polyhedron, which is the union of a sphere and polyhedron based on the Minkowski sum, as illustrated in Fig. 3(b). The dilation radius of the sphere controlled the smoothing of the dilated polyhedron, and it was set to 10% of the average particle size in the bonded model.

4.1. Bond model

In this model, a vector $\mathbf{d}$ connects two bonded points, denoted as i and j. The unit normal vector to the surface of the bond is defined as $\mathbf{n} = \frac{\mathbf{n}_i - \mathbf{n}_j}{|\mathbf{n}_i - \mathbf{n}_j|}$, where $\mathbf{n}_i$ is the outward normal to the surface at the position of point i, while $\mathbf{n}_j$ is the outward normal at the position of point j. To calculate the normal strain ε in the bond, the reference length $l_{ij} = l_i + l_j$ was introduced as the sum of the distances from the center of each element to the interface of the element (Liu and Ji, 2019). The normal strain can then be expressed as

$$\varepsilon = \frac{\mathbf{d} \cdot \mathbf{n}}{l_{ij}}. \tag{5}$$

Utilizing the additive decomposition of $\mathbf{d}$ into the normal $\mathbf{n}$ and tangential direction $\mathbf{t} = \frac{\mathbf{d} - (\mathbf{d}\cdot\mathbf{n})\mathbf{n}}{|\mathbf{d} - (\mathbf{d}\cdot\mathbf{n})\mathbf{n}|}$, the engineering shear strain in the bond

is described as

$$\gamma = \frac{|\mathbf{d} - (\mathbf{d}\cdot\mathbf{n})\mathbf{n}|}{l_{ij}} \tag{6}$$

Given the strains in the bond, the stresses are calculated using a constitutive relationship, in this case, Hooke's generalized law, i.e.,

$$\sigma = \frac{E(1-\nu)}{(1+\nu)(1-2\nu)}\varepsilon = k_n\varepsilon, \tag{7}$$

$$\tau = \frac{E}{2(1+\nu)}\gamma = k_t\gamma, \tag{8}$$

where E represents Young's modulus, ν stands for Poisson's ratio, σ denotes the normal stress and τ represents the shear stress.

Given the stresses in the bond, the Cauchy traction vector reads $\mathbf{T} = \sigma\mathbf{n} + \tau\mathbf{t}$. The magnitude of the Cauchy traction vector represents the effective stress,

$$\sigma_e = \sqrt{\langle\sigma\rangle^2 + \tau^2}, \tag{9}$$

while

$$d_e = \sqrt{\langle d_n\rangle^2 + d_t^2} \tag{10}$$

is the corresponding magnitude of the displacement vector $\mathbf{d}$, where $d_n = \mathbf{d}\cdot\mathbf{n}$ and $d_t = \mathbf{d}\cdot\mathbf{t}$. Here, $\langle\,\rangle$ denotes the Macaulay brackets excluding the compression stress and displacement, i.e.,

$$\langle\sigma\rangle = \begin{cases} 0, & \text{if } \sigma < 0 \\ \sigma, & \text{if } \sigma \geq 0. \end{cases} \tag{11}$$

At the onset of damage in the bond, the quadratic nominal stress criterion (QNSC) is assumed as

$$\left(\frac{\langle\sigma\rangle}{\bar{\sigma}}\right)^2 + \left(\frac{\tau}{\bar{\tau}}\right)^2 = 1, \tag{12}$$

where $\bar{\sigma}$ represents the tensile strength, and $\bar{\tau} = C - \mu\sigma$ represents the Mohr–Coulomb shear strength. Here, C represents the cohesion of the material, and $\mu = \tan\phi$ represents the internal friction coefficient, with ϕ denoting the angle of internal friction for the material.

To describe the evolution of damage in the bond, an irreversible Kachanov-like damage variable denoted as $D \in [0, 1]$ was introduced. Linear softening is considered, which can be expressed as follows

$$D = \frac{d_e^f\left(d_e^{max} - d_e^0\right)}{d_e^{max}\left(d_e^f - d_e^0\right)}, \tag{13}$$

where d_e^0 represents the effective displacement at the onset of damage, d_e^f stands for the effective displacement at rupture (i.e., $\sigma_e = 0$) and d_e^{max} corresponds to the maximum attained value of the effective displacement in the loading history. The area of the triangle beneath the effective traction–separation law, denoted as G_f, and the effective stress at damage initiation, denoted as σ_e^0, determine the effective displacement at rupture as follows

$$d_e^f = \frac{2G_f}{\sigma_e^0}. \tag{14}$$

An illustration of the effective traction–separation law is depicted in Fig. 4. A commonly employed expression for G_f is derived from the work of Benzeggagh and Kenane (1996). This expression is given by

$$G_f = G_I + (G_{II} - G_I)\left(\frac{2G_{II}}{G_I + 2G_{II}}\right), \tag{15}$$

where G_I represents the area under the mode I traction–separation law in pure tension, while G_{II} represents the area under the mode II traction–separation law in simple shear. The fracture energy required to break the bond is defined as the area beneath the force–displacement curve, rather than the traction–separation law, although they are connected through the bond's cross-sectional area.

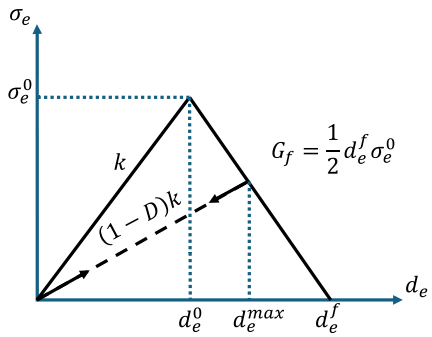

Fig. 4. Traction–separation law.

As the damage variable D increases from 0 to 1, the stresses in the bond degrade as follows

$$\sigma = \begin{cases} \frac{k_n}{l_{ij}}d_n, & \text{if } d_n < 0 \\ (1-D)\frac{k_n}{l_{ij}}d_n, & \text{if } d_n \geq 0, \end{cases} \tag{16}$$

$$\tau = (1-D)\frac{k_t}{l_{ij}}d_t. \tag{17}$$

In other words, there is no damage in compression, i.e., $d_n < 0$. Consequently, the particles may overlap at the contact points undergoing compression. The amount of overlap is controlled by the stiffness $\frac{k_n}{l_{ij}}$. Upon bond breakage (i.e., $D = 1$), the bond, along with its associated force and stiffness, is removed. Subsequently, the Hertz–Mindlin contact model (Nye et al., 2014) remains, using the dilatation radius of the dilated polyhedron instead of the spherical particle radius.

To remedy traction oscillations, the presented formulation requires a special computational procedure because it is based on an explicit method, as summarized in Algorithm 1.

Algorithm 1

1. Initialize a flag variable "init" as "True."
2. Calculate displacements using Eqs. (5) through (6) and (10).
3. Calculate stresses using Eqs. (7) through (9).
4. If QNSC equals 1 and "init" is "True," define d_e^0, σ_e^0, d_e^f, and set "init" to "False." **Remark 1.1**: If $d_e^f \leq d_e^0$, set $d_e^f = d_e^0$ + tolerance and update G_f according to Eq. (14).
5. If "init" is "False," calculate the damage variable using Eq. (13) and update stresses using Eqs. (16) through (17) and (9). **Remark 1.2**: If $d_e^{max} > d_e^f$, set $D^{(n+1)}$ to 1. **Remark 1.3**: If $D^{(n+1)} < D^{(n)}$, set $D^{(n+1)} = D^{(n)}$.

Given the stresses in the bond, the normal force F_n and the shear force F_t are calculated as the normal stress σ and the shear stress τ acting on the bond area $\frac{A}{n}$, respectively, where A represents the area of the interface, and n stands for the number of bonds on the interface. The fracture energy needed to break the interface is the sum of the area under the force–displacement curves of the bonds.

To dissipate some of the kinetic energy and thereby improve the stability of the bonded DEM model, a damping coefficient β proportional to the stiffness of the bond and the strain rate, resembling a standard dash-pot (Jou et al., 2019) was introduced. This is expressed as follows in Eqs. (18) and (19)

$$F_n = \left(\sigma - \beta k_n\dot{\varepsilon}\right)\frac{A}{n}, \tag{18}$$

$$F_t = \left(\tau - \beta k_t\dot{\gamma}\right)\frac{A}{n}. \tag{19}$$

Note that the forces in Eqs. (18) and (19) are calculated in the local coordinate system defined by the orientation of the bond surface. These

forces must be transformed to the global coordinate system as follows

$$\mathbf{F} = F_n\mathbf{n} + F_t\mathbf{t}, \tag{20}$$

where **n**, **t**, and **d** are all expressed in the global coordinate system.

The final step involves vector addition to determine the force and moment acting on each particle before updating the orientations and positions of the particles by using Newton's second law.

5. Model calibration

5.1. FEM model calibration

3D Brazilian disc test (BDT) simulations were performed in the same way as in the experiments by first ensuring contact between the loading plates and the cylindrical mineral sample, followed by monotonic loading until failure. For single particle breakage (SPB) simulations, because of the irregular shape of the 3D scanned samples and the optimization of the contact points with the loading plates during compression, settlement simulations using the effect of gravity were implemented as a pre-loading stage. In contrast to the compressive loading stages, the settlement simulations used a dynamic implicit time-integration method. The resting bodies were then monotonically loaded in a displacement-control setting. The displacement rates were scaled to obtain a reasonable computational time. Although the deformation rates were increased and the velocity of the plates was set to 10 mm/s, they were sufficiently low to neglect the inertial dynamic effects. The results were verified by testing different velocities and evaluating the contribution of dynamic effects on the mechanical response. In both the BDT and SPB models, it was assumed negligible the deformation of the plates.

The BDT model consisted of a cylindrical sample (D = 44.8 mm, t = 13.8 mm) with eight-node brick elements with reduced integration, loaded along its diameter using two flat rigid plates. For the SPB simulations, reconstructed 3D scanned samples of different shapes and sizes were used. The geometries were meshed with ANSA BETA CAE systems v24 using a combination of 4-node linear tetrahedral and 5-node pyramidal elements to obtain both good resolution and computational cost. The distribution of the element volume of the 3D scanned rocks during the meshing process of the BDT geometries was considered for consistency during calibration. The size dependency in fracture mechanics simulations is acknowledged; however, in this model, the definition of the probability of failure and defect density by means of a Weibull distribution reduces its effect on the overall mechanical response. Furthermore, a workflow was implemented to address the mesh-size-dependent fracture energy by accounting for the same characteristic volumes across the models. The BDT samples had 188,000 elements, whereas the 3D scanned rocks had 110,000–210,000 elements due to different volumes.

It has been demonstrated that for Brazilian disc tests, there is a minimal difference between friction and frictionless setups in the stress distribution within the central area of the disc where the stresses are fully developed (Yuan and Shen, 2017). However, at the contact points, the radial and tangential components of the stress are higher when there is no physical buffering of the rough contact between the plates and disc, such as through cushioning techniques. In the present simulations, to simulate the experimental setup as accurately as possible without compromising the computational cost, a kinematic contact constraint was implemented in ABAQUS, allowing some separation in the normal direction with a HARD pressure definition, while employing a penalty definition with $\mu = 0.6$ in the tangential direction.

5.1.1. Calibration result

Figs. 5(a) and 5(b) present the force–displacement response of the granite and limestone Brazilian disc samples. Slight nonlinearities in the experimental data can be attributed mainly to defects in the material but also to the concentration of stresses close to the contact points and frictional effects. Although granite and limestone have different morphologies, a similar initial stiffness of the sample was identified and was used to determine the Young modulus E of the two materials instead of performing additional uniaxial compression tests solely for this purpose. Due to this similar initial stiffness, the same value of Young's modulus will be used for both materials, resulting in decent agreement with the experimental force–displacement graphs in Figs. 5(a) and 5(b). For the other parameters in the KST-DFH model, the calibrated parameters in Saadati et al. (2014) for Bohus granite were used as a starting point in the present work.

Focus for the calibration of the model with the present materials is to capture the failure load statistics of the Brazilian disc samples. Statistical distributions of failure loads, both from simulations and experiments, were estimated using median ranks. The calibration showed that it was sufficient to change only the Weibull parameters σ_w and m to obtain decent agreement with the experimental data as seen in Fig. 6. The same Weibull exponent $m = 7$ was found to describe the outcome of both materials while the Weibull stress differed with $\sigma_w = 17$ MPa and $\sigma_w = 21$ MPa for limestone and the granite materialm, respectively. The KST part of the model has a very limited influence on the results for the Brazilian disc load case, and hence the material parameters determined in Saadati et al. (2014) were used for both materials. This statement will be validated later when simulating the single particle breakage test. All needed material parameters, both presently calibrated and those taken from Saadati et al. (2014), are presented in Table 1.

Figs. 5(c) and 5(d) show the fracture patterns of both granite and limestone. The damage variable D_1 indicates the maximum level of damage in the first principal direction when it reaches unity (blue if $D_1 = 0$, red if $D_1 = 1$). The physical meaning of this value is related to the open cracks that are normal to the maximum principal stress direction. The FEM results show good agreement with the fracture pattern: a main crack along the loading direction and secondary cracks at the contact points due to shear stresses.

A parametric study was performed to determine the sensitivity of the Weibull modulus m and average strength σ_w on the expected failure load values. Both strong and weak specimens were included in the results looking to replicate heterogeneity of the source material in comminution processes. (Notice that here the terms weak and strong refer to a scale of rock strength.) The cumulative density function of the failure loads in Fig. 6, estimated using median ranks, shows a large scatter in the data for both granite and limestone. Simulations were performed using different combinations of characteristic parameters and determined that the Weibull modulus and average strength are interdependent parameters contributing to dispersion of the failure load.

Data from numerical simulations have less scatter than the experimental data, that is, there is a probability of underestimating the failure load of strong specimens. The Brazilian disc is a practical test for obtaining the tensile response of brittle materials, however, it is important to highlight the complexity of the stress state and mechanics at the contact points. Deterministic behaviors become dominant when high compressive stresses close to the contact point activate random defects and contribute to damage in the principal direction; thus, there is a loss in the stiffness of the element and overall failure of the continuum.

5.2. DEM model calibration

First, the Brazilian disc was discretized into 300 cells using a pruning distance of 2.5 mm in Demify. To accelerate the simulations, the velocity of the top plate was set to 250 mm/s. The time step

Table 1
Parameters used in the KST-DFH material model. For the KST part, the parameters in Saadati et al. (2014) for Bohus granite were used for both materials.

			Granite	Limestone
		Mechanical Properties		
	E	(GPa)	77	77
	ν	(–)	0.21	0.21
	ρ	(kg/m^3)	2540	2540
KST		Hydrostatic behavior(from Saadati et al. (2014))		
	$\varepsilon_v^{(n)}$	(–)	[0, −0.028]	[0, −0.028]
	$P^{(n)}$	(MPa)	[0, 864]	[0, 864]
		Deviatoric behavior (from Saadati et al. (2014))		
	a_0	(MPa)^2	23 500	23 500
	a_1	(MPa)	465	465
	a_2	(–)	1.51	1.51
DFH		Weibull parameters		
	m	(–)	7	7
	σ_w	(MPa)	21	17
	V_{ref}	(mm^3)	195	195

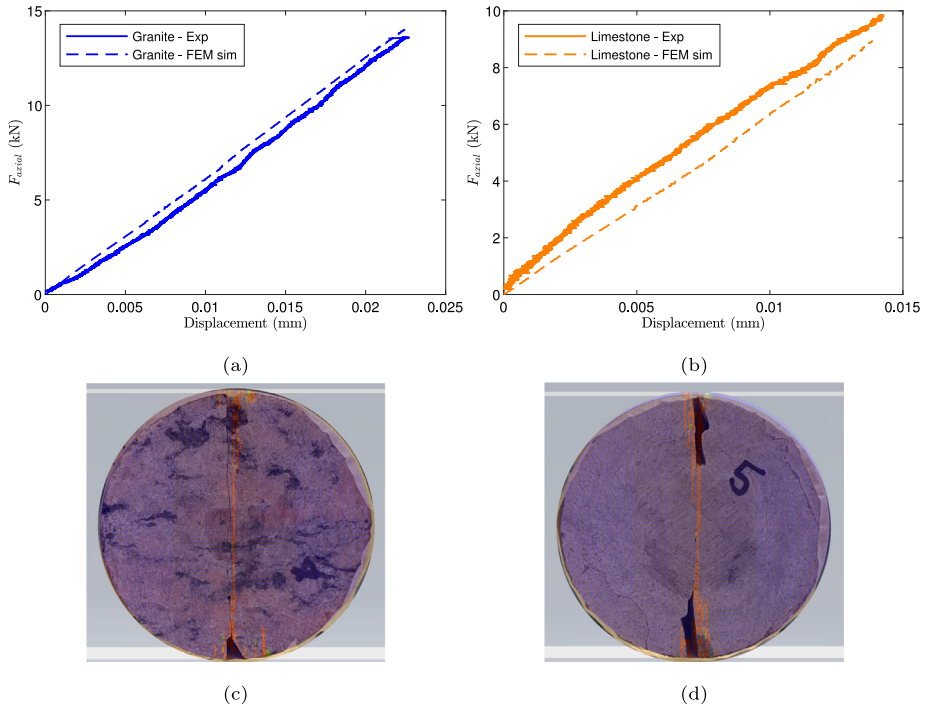

Fig. 5. Qualitative and quantitative results of granite (left) and limestone (right) Brazilian disc samples. Figure (a–b) presents the force–compression response for both experiments (obtained via virtual extensometer l) and simulations. Figure (c–d) presents an overlay of post-fracture images from experimental results and post-failure damage obtained from simulations (blue if $D_1 = 0$, red if $D_1 = 1$). (For interpretation of the references to color in this figure legend, the reader is referred to the web version of this article.)

size is 1×10^{-7} seconds, corresponding to 0.0171 times the Rayleigh critical time step, using the average particle size of 5.5 mm in the 300-cell model. A design of experiments (DOE) on inputs that have the most significant influence on the model's behavior was performed to assess the impact of model inputs on model outputs (Yoon, 2007). This approach enabled the optimization of the model's performance relative to the experimental results, where the target values were the average maximum force and the corresponding displacement between the two contact points in Fig. 1(a). The model inputs of significant influence were assumed to be the Young's modulus of the bond, the bond's tensile strength (with cohesion set to 1.5 times the tensile strength Ma et al., 2014), and the internal friction coefficient. The remaining fixed model inputs are presented in Table 2. As previously pointed out, Young's modulus was not measured but was instead treated as a calibration parameter in both DEM and FEM. Additionally, a rock–steel friction coefficient of 0.95 was used to mitigate sliding in the simulations. Two expressions were obtained: one for the maximum force (with a coefficient of determination $R^2 = 0.98$) and one for the corresponding displacement (with a coefficient of determination $R^2 = 0.9$), as functions of model inputs that significantly influence the system. Subsequently, the errors were minimized from the target values through multi-objective optimization using a weight factor of 0.5. The calibration results for granite and limestone are presented in Table 3 and Fig. 7(a). Although the maximum force remained within the measured experimental range, the corresponding displacement did not. This discrepancy can be attributed to the coefficient of determination $R^2 = 0.9$ for the expression derived from the DOE for the displacement at maximum force, in contrast to $R^2 = 0.98$ for the maximum force itself, combined with multi-objective optimization. Moreover, more advanced methods for parameter identification, such as machine-learning techniques, are available for this class of problems (Ibrahimbegovic et al., 2020; Dobrilla et al., 2023a,b), which represent a highly active

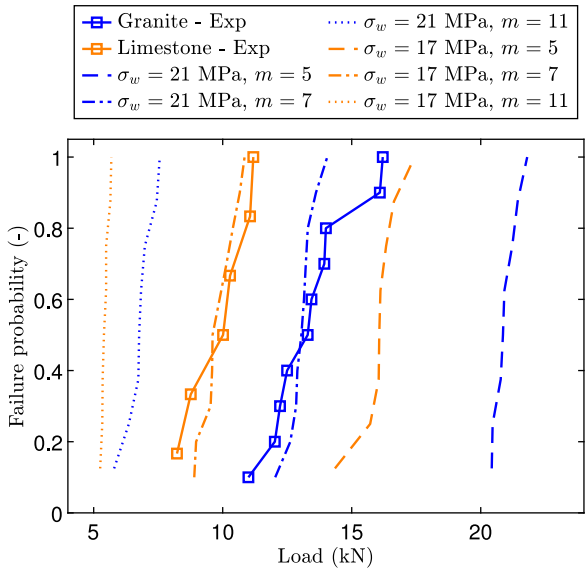

Fig. 6. Cumulative density function (CDF) of failure loads of granite and limestone Brazilian samples illustrating the effect of the Weibull parameters m and σ_w on the failure load, as well as the calibrated parameters with a point-dashed line.

Table 2
DEM material and contact model parameters.

Rock	
Young's modulus	77 GPa
Poisson's ratio	0.21
Density	2540 kg/m^3
Steel	
Young's modulus	210 GPa
Poisson's ratio	0.3
Density	7700 kg/m^3
Rock–Rock	
Sliding friction	0.6
Coefficient of restitution	0.15
Rock–Steel	
Sliding friction	0.95
Coefficient of restitution	0.3
Bond	
Poisson's ratio	0.25
Damping coefficient	1×10^{-4}
Mode I area	10 N/m
Mode II area	10 N/m

Table 3
Calibrated DEM bond parameters for granite and limestone.

Parameter	Granite	Limestone
Young's modulus	43 GPa	46 GPa
Tensile strength	38 MPa	28 MPa
Cohesion	57 MPa	42 MPa
Internal friction	0.8	0.8

field. Nonetheless, the calibrated result was assumed to be satisfactory in capturing the mechanical response of granite and limestone, given the experimentally observed variance and in comparison to comminution modeling, where it is common practice to set the particle stiffness lower than the actual rock stiffness to speed up DEM simulations, as pointed out by Delaney et al. (2015).

Another important aspect of calibration, alongside curve fitting, is ensuring that the simulation adequately reflects what is observed in the experiment. Fig. 7(b) illustrates the damage evolution in the Brazilian disc. In this visualization, the red cell indicates that all bonds have failed, whereas the darkest blue cell indicates that no bonds have failed. Ideally, a splitting crack should be initiated at the center of the disc for the tensile test to be accurate. However, this is rarely the case as initiation often deviates from the center and may even start from the loading plates (Fairhurst, 1964). Cracks originating from the loading plates are more common in tests utilizing flat loading plates, primarily because of the stress concentration associated with point loads. Nevertheless, the predicted crack path in Fig. 7(b) aligns well with that in other studies (Ma and Huang, 2018; Wessling et al., 2022).

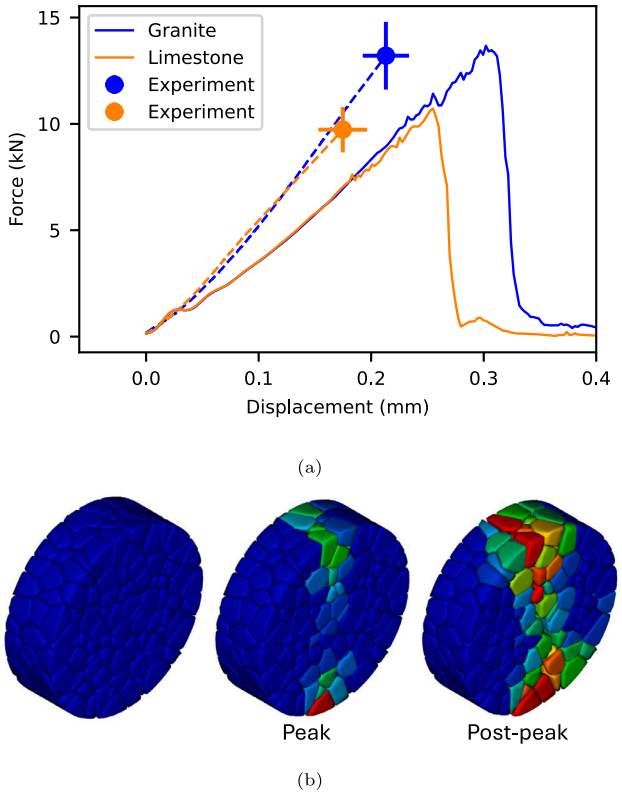

Fig. 7. (a) Calibrated force–displacement response of a Brazilian disc of granite and limestone, along with the upper and lower measured bounds. (b) Damage evolution in a Brazilian disc, where the red cell represents all bonds having failed, and the darkest blue cell indicates that no bonds are failing. (For interpretation of the references to color in this figure legend, the reader is referred to the web version of this article.)

5.2.1. Mesh dependency

The objective is to simulate the industrial-scale crushing of rocks towards comminution, a process involving large-particle systems. Naturally, this imposes constraints on the number of cells in a bonded DEM model considering that the critical time step is proportional to the particle size (Burns et al., 2019). Additionally, this model is currently restricted to a finite array of unique particle shapes (up to approximately a thousand unique element shapes). In principle, the prediction ability will be improved by a more resolved mesh in both the particle scale simulation as well as in the system scale. The trade-off between local resolution for each particle and the number of feed particles has yet to be decided case by case. Therefore, it is relevant to investigate the mesh resolution dependency on the fracture response on the particle scale. Fig. 8 illustrates the tensile strength of the Brazilian disc plotted against the number of cells, indicating that it was within an acceptable range for attaining mesh convergence. The meshing parameters used to discretize the disc are listed in Table 7.

To extend a given mesostructure from the Brazilian disc to irregular geometries, such as rocks, the relative measure V_{BDEM}/n_{cells} was introduced, where V_{BDEM} represents the volume of the bonded DEM model,

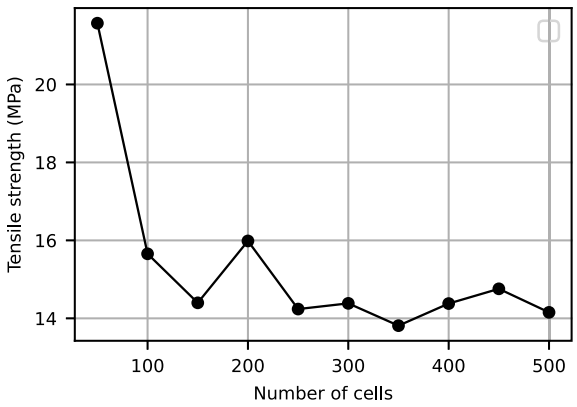

(a)

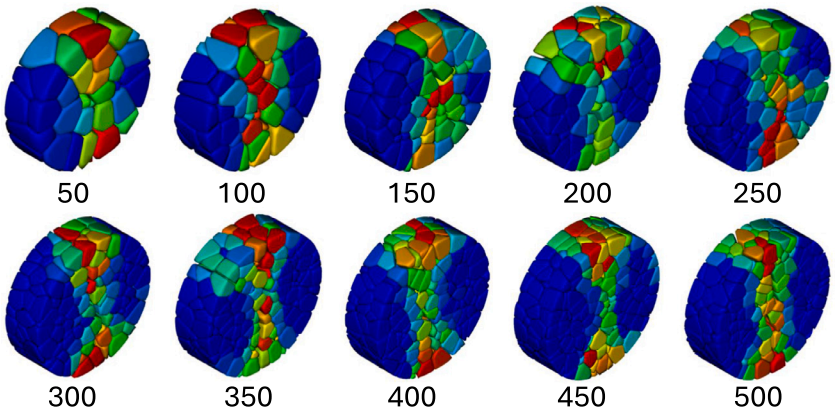

(b)

Fig. 8. Tensile strength of the Brazilian disc as a function of the number of cells, and the post-peak damage distribution in the disc (red cell indicating all bonds have failed, darkest blue cell indicating no bonds are failing). (For interpretation of the references to color in this figure legend, the reader is referred to the web version of this article.)

and n_{cells} denotes the number of cells. This measure should remain consistent across the bonded DEM models, ensuring uniformity in the average mesostructure across all geometries. This is refered to as the meso constant.

5.2.2. Rate dependency

The Brazilian disc was subjected to various loading rates to explore the rate-dependent behavior resulting from the term with damping coefficient β in Eqs. (18) and (19). Fig. 9 illustrates the force–displacement response of the disc for different loading rates, calculated as the velocity of the plate divided by the diameter of the disc. The previously applied plate loading velocity of 250 mm/s corresponds to a loading rate of 5.6 per second. It was observed that as the loading rate increases, the softening response of the force–displacement curve transitions from a rapid to a more gradual drop. This behavior is expected because the strain rate is proportional to the damping coefficient in Eqs. (18) and (19). The strength of the disc remains unaffected because cracks propagate at high speeds during the softening part of the curve, often approaching the speed of sound in brittle materials. The rapid propagation of cracks in brittle materials is associated with the release of the stored elastic energy.

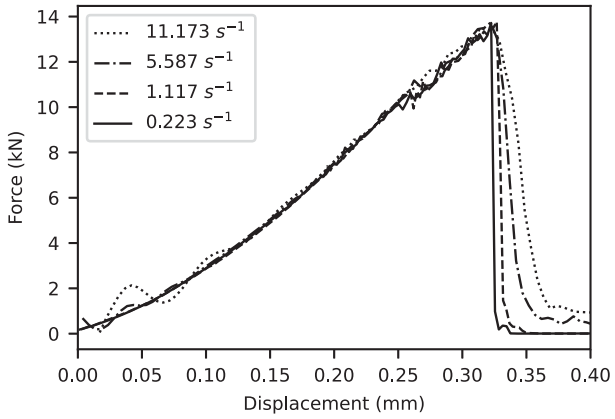

Fig. 9. The force–displacement response of a Brazilian disc of granite under different loading rates.

6. Single particle breakage simulations

6.1. FEM simulation results

Once the material parameters $m, \sigma_w, \sigma_{coh}$ were calibrated against Brazilian disc experiments, numerical simulations of single particle breakage (SPB) tests were used to validate the mechanical response of a few randomly selected irregularly shaped samples using the same material parameters as in the Brazilian disc simulations. Fig. 10 presents the results of the cumulative density function of the failure load for both the experiments and simulations of the granite and limestone samples. The numerical results were in good agreement with the experimental data. In comparison to the results from Brazilian disc simulations, there

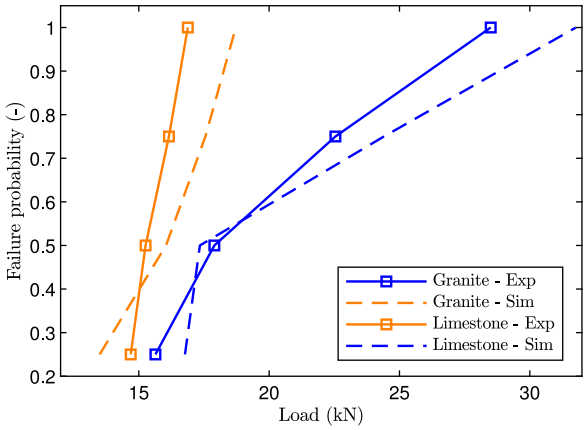

Fig. 10. Cumulative density function (CDF) of failure loads of irregularly shaped granite and limestone samples comparing experimental outcomes with predictions using FEM.

is a higher probability of overestimating the failure load of rock samples with FEM simulations.

To obtain an accurate description of the mechanical response and fracture pattern, the load–displacement curves were also checked. Fig. 11(a) shows the experimental and numerical results for the granitic rock sample. The overall behavior of the experiments and simulations is similar with an increasing load until failure at approximately 20 kN, where the load drops suddenly due to the propagation of a major crack. The slight instabilities during loading can be attributed to crumbling (Tavares, 2007) and local microcracking during the loading process. Differences might be caused by disparities in the initial positioning of the rocks. Fig. 11(b) presents the load–displacement response of a limestone rock sample and, as for granite, the FEM simulation captures the failure load and overall process.

The fracture pattern was well captured by the simulations (see Figs. 11(c) and 11(d)) compared to the experimental results (see Figs. 2(a) and 2(c)). Small rotations and chipping at the contact points during compression experiments were also observed in the simulations. Although a higher resolution at the contact points can provide a more accurate response, it also negatively affects the computational cost.

Brazilian disc tests included both strong and weak samples, which increased the scatter of the failure load. The scatter obtained from the numerical simulations is not as large as that obtained from the experimental tests, which can lead to underestimation of the failure load. However, the validated data from the single particle breakage tests showed great agreement, and the trend in the scatter was well captured. From a statistical point of view, geometry plays an important role in the prediction of the detailed fracture behavior under compressive loads. The reason for this is the relationship between the number of contact points, heterogeneity of the mineral material, and random distribution of defects. High stresses activate flaws in the material until it reaches a critical state in which damage in the material counteracts the ability to withstand further loading.

6.2. DEM simulation results

In the discretization of the rocks from granite and limestone, a meso constant of 2.2×10^{-7} was utilized, corresponding to 100 cells in Fig. 8, to expedite the large-scale crushing simulation, while ensuring detailed predictions of the crack path within the rocks. The meshing parameters used to discretize the rocks are listed in Table 7. Due to the significant computational expense associated with simulating an almost quasi-static experiment with an explicit solver, the plate velocity applied was 50 mm/s (equivalent to a loading rate of 1.117 s^{-1} in Fig. 9) to accelerate the simulations. Fig. 9 shows that the loading rate does not affect the load-bearing capacity of the DEM model. Figs. 12(a) and 12(b) show the force–displacement responses of the DEM simulations and experiments for granite and limestone, respectively. The crack predictions, along with the meshed rock, are displayed after the initial fracture event in Figs. 13(a) and 13(b), which were identified by the first notable drop in force. It is important to remember that the DEM simulations were calibrated against the Brazilian disc test in Fig. 7(a) and not against the single particle breakage experiments. The predicted slope and maximum force in the DEM simulations exceeded the experimental values, whereas results of the crack path predictions, depicted in Figs. 13(a) and 13(b), align with the experimental recordings considering the coarse mesh used.

Considering that the calibrated DEM model is less stiff than the Brazilian disc, it is a noteworthy observation that the opposite is observed in the single particle breakage case. Compared to the Brazilian disc, which exhibits a splitting-like crack through the specimen, the single particle breakage test shows shape effects in the form of crumbling (i.e., local contact damage), a precursor to crack propagation. This mechanism can also be confirmed by examining the force–displacement response of the single particle breakage test, which is nonlinear, compared to the almost linear response of the Brazilian disc test. The DEM model does not capture this local mechanism due to mesh coarseness, while the high-resolution FEM model does, which is a trade-off when making the DEM scalable. A comparison between FEM, DEM and the experiments is presented in Section 7.

7. Discussion and comparison

In Fig. 14, the failure probability distributions from the single particle breakage tests are shown for the DEM simulations and compared with previous FEM and experimental results. A larger variation is observed in the simulations compared to the experiments. Overall, the DEM simulations tend to overpredict the failure load, whereas the FEM results are much closer to the experimental values, although they are generally about 10% higher than the experimental results. It is also worth noting that the experimental curve differs somewhat from the one shown in Fig. 10. In Fig. 10, only the experimental points used to validate the FEM model were included in the curve, while in Fig. 14, the full experimental dataset is utilized.

Fig. 15 shows a comparison of the crack patterns for both granite and limestone using different methods: DIC, FEM and DEM simulations. The major cracks responsible for failure are well captured by both numerical methods, although FEM simulations are also able to capture secondary cracks. However, comparing the DEM and FEM crack predictions directly is difficult due to differences in mesh resolution and, consequently, model geometry, as well as the current DEM implementation of averaged damage variables for Voronoi cells, which prevents plotting exact crack paths. As a result, only general crack patterns can be shown, not precise locations, though the overall trends in crack patterns appear to overlap between the two models.

Unlike FEM, where an element stops contributing once the damage variable reaches one, in the bonded DEM, the Hertz–Mindlin contact model remains. It contributes to the load increase until the first fracture event occurs, resulting in the separation of the rock into two or more parts. Additionally, due to the use of a coarse DEM mesh that enables upscaling, capturing crumbling (Unland, 2007) (local contact damage) is more challenging than in FEM. In the Brazilian test, crumbling was not an issue, as indicated by the linear curve up to the failure point. Crumbling causes flattening or widening of the contact region, redistribution of stresses in the rock, and explains the stiffening force–displacement response of the rocks. Capturing this phenomenon requires significantly more discrete elements, which would substantially increase the computational cost of the large-scale simulation and make it infeasible. Another contributing factor to the crumbling mechanism is the non-convex rock shape which was approximated by the convex hull method in Fig. 3(a).

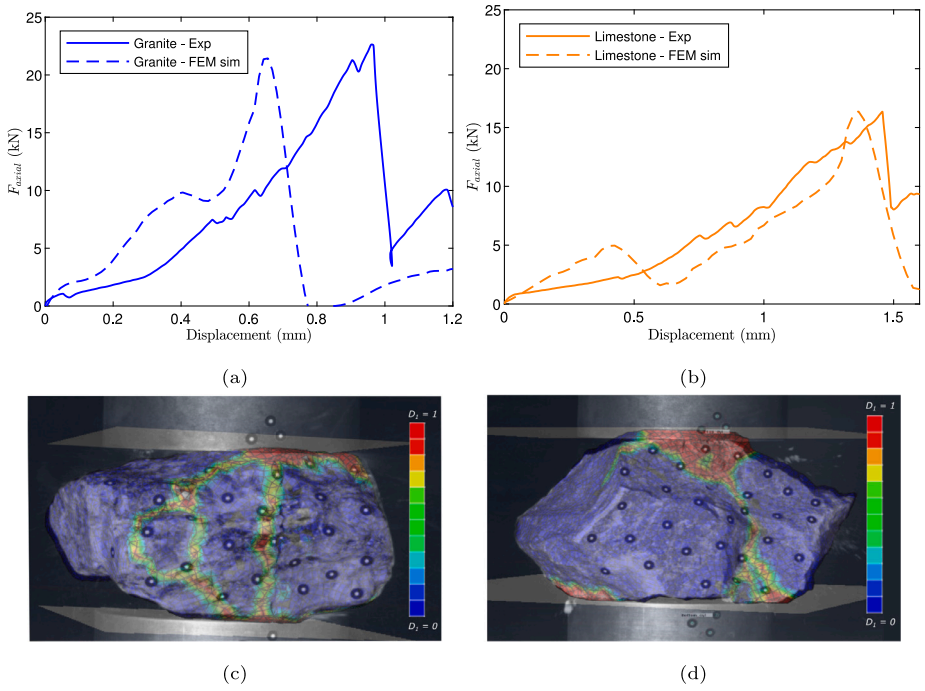

Fig. 11. Qualitative and quantitative results for granite and limestone samples. Figures (a) and (b) present the force–displacement response for both the experiment (obtained via an external extensometer) and the simulation of granite and limestone samples, respectively. Figures (c) and (d) present an overlay of the post-fracture pattern from the experimental results and the damage obtained from the simulations of granite and limestone samples, respectively.

8. Demonstration of the DEM model for a cone crusher application

As the work in this paper relates to the 'industrial scale' of a comminution system in relation to the particle scale, it is relevant to address a suitable definition of the term. The following aspects can be considered:

- The machine system size as well as size ratio to the representative size of the particle population.
- The number of particles needed in a model of such a system.
- The prediction utility of the performed simulation. The utility may either be related to the ability of predicting machine related responses such as power draw, wear, capacity etc. It can also mean the ability to predict the particle material response in terms of particle size distribution, fracture rates, particle shape, or even mineral liberation. The ideal ability is naturally that both machine and material responses can be predicted with an accuracy enough to improve the system or solve a particular problem.

In this section, we demonstrate the proposed methodology on a typical cone crusher model used in aggregate production and mining operations. The cone crusher machine operates such that the mantle is assembled on the main shaft, which is seated in an eccentric bushing at the bottom and held by a plain bearing at the top of the shaft. When the eccentric bushing is turned, the mantle moves in a nutating motion with a pivot point in the top bearing, causing an opening and closing compression action between the mantle and the concave surfaces. As the particles flow further down in the chamber the distance between the surfaces reduces and the particles are sequentially fractured. The mantle can be lifted up and down through a hydraulic cylinder, enabling control of the close side setting (CSS). The CSS is defined as the smallest gap between the mantle and the concave at the end of the chamber. The eccentric throw is given by the eccentric bushing and can hence not be controlled or adjusted during operation.

The crusher machine model used for the demonstration is a Sandvik Hydrocone CH660 with a coarse chamber. The system domain size to fit the crusher is approximatly L2 × W2 × H3 meter. The machine and operating parameters are summarized in Table 4. The crusher was operated with eccentric speed 290 rpm, close side setting at 38 mm, eccentric throw 26 mm and a uniform feed size between +60/−90 mm. A choke feeding condition is created by initiating the feed with a plane geometry at the choke level position in the chamber for the first second of feeding. The plane is then lowered and the crushing is initiated. This start sequence allows for a fast reach of steady-state operation. The feed particle model of rock 7 made of granite is meshed with 198 Voronoi elements and the material and bond model parameters for granite seen in Tables 2 and 3 are applied. The results for the demonstration simulation can be seen in Fig. 16. The mean power draw is ~146 kW, the mean hydrostatic pressure is 1.22 MPa and the throughput is 199 tons per hour (tph). In this work, we will not compare the simulation results to experimental results since such a scope would suit a separate publication. However, the resulting nominal values for mass flow throughput, power draw and hydrostatic pressure are in the right order of magnitude and well in line with the typical expected values seen in the Sandvik manual for the CH660 crusher model.

Table 4
Parameter settings for the cone crusher simulation case. The DEM parameters for granite, which is considered in this case, are listed in Tables 2 and 3.

Parameter	Value	Unit
Closed side setting	38	[mm]
Eccentric throw	26	[mm]
Ecentric speed	290	[rpm]
Feed size distribution	+60/−90	[mm]
Concave type	Coarse (C)	[–]
Crusher model	CH660	[–]

The calculation of the fragment size distribution from a bonded element particle model is not trivial. Quist and Evertsson (2016) applied an image analysis-based approach to estimate the size distribution. Here, an alternative approach is used to identify the connectivity of all surviving fragments for each time sample event. The characteristic particle size for each fragment is then calculated for the cluster of intact Voronoi elements making up a fragment particle. The resulting feed,

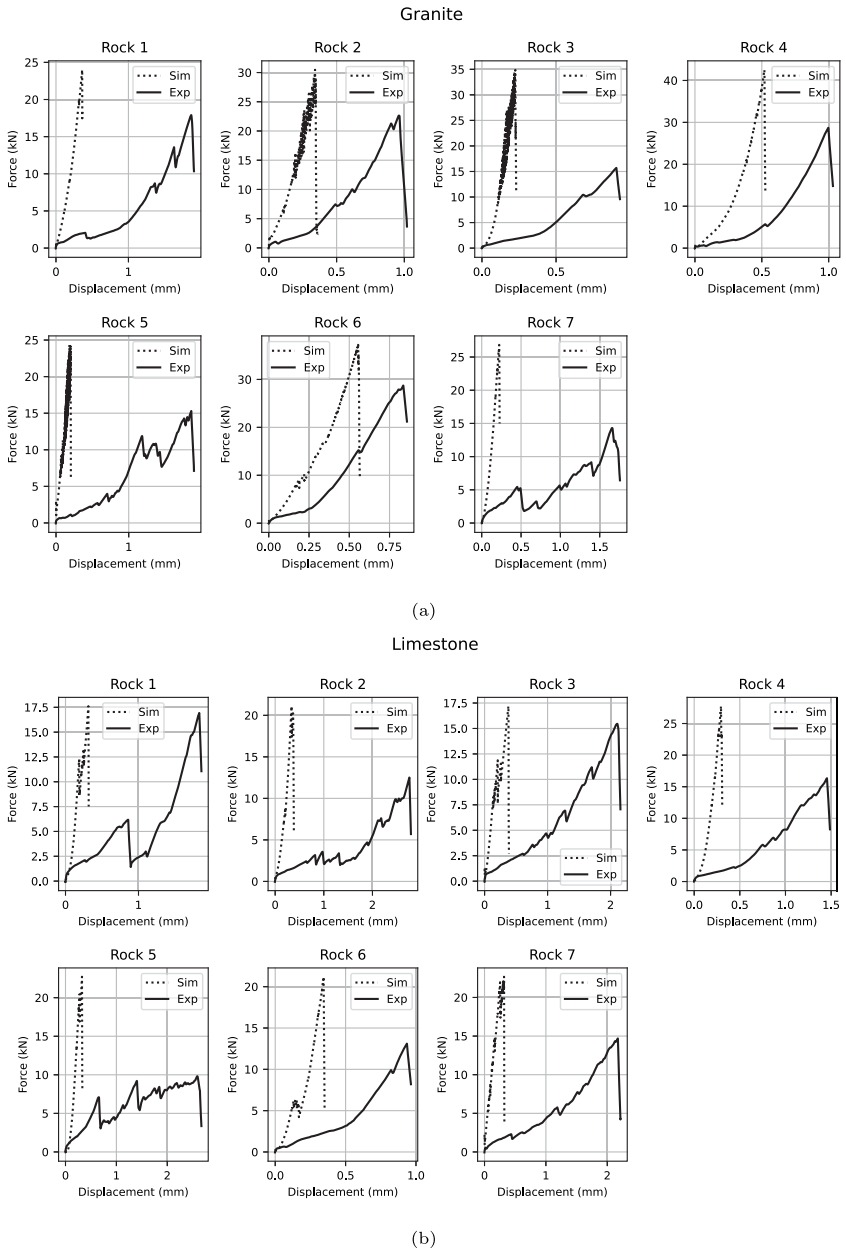

Fig. 12. Comparison between the force–displacement response of single particle breakage from DEM simulations and experimental curves for (a) granite and (b) limestone.

discharge and Voronoi element particle size distributions are presented in Fig. 16. For cone crusher applications it is a rule of thumb that the P80 particle size should be within some millimeters of the value of the close side setting. Here, the P80 equals 41.2 mm and the CSS is 38 mm, which indicates that the simulated crushing response is realistic.

An important observation is that the Voronoi fragment size distribution provides a constraint on the fine end of the discharge product size distribution. Furthermore, if a single Voronoi mesh resolution is used for all feed particle sizes, the element top size for the largest feed size constrains the closed-side setting. A solution to this problem is to generate more resolved meshes for the largest feed particles and less resolved meshes for the smallest feed particles. This also has the benefit of controlling the effective element distribution within a narrow range. The computational performance in terms of simulation time was ~ 500 min per simulated second for the steady-state operation at a time step of 2.5e−7 s and 119,600 particle elements active in the domain. The memory allocation on the GPU was ~ 3600 MB. A system with approximatly 6 times larger particle population size would be possible on the same graphics card with 24 GB memory available. The model was configured with a constant feed rate and a particle destructor domain below the crusher; hence, the total cumulative number of elements passing the crusher was higher and proportional to the simulation end time. The simulation was performed on a workstation with an Nvidia RTX3090 graphics card and AMD Ryzen 9 7950X 16-core processor. Hence, it is deemed that these simulations are feasible from an industrial perspective as useful results can be obtained overnight on a high-end workstation.

9. Conclusions

The major outcomes of the work can be summarized as follows:

- The calibration of the bonded Voronoi-based DEM model and the KST-DFH rock mechanics material model in FEM was performed using the Brazilian disc test with a known cylindrical rock shape

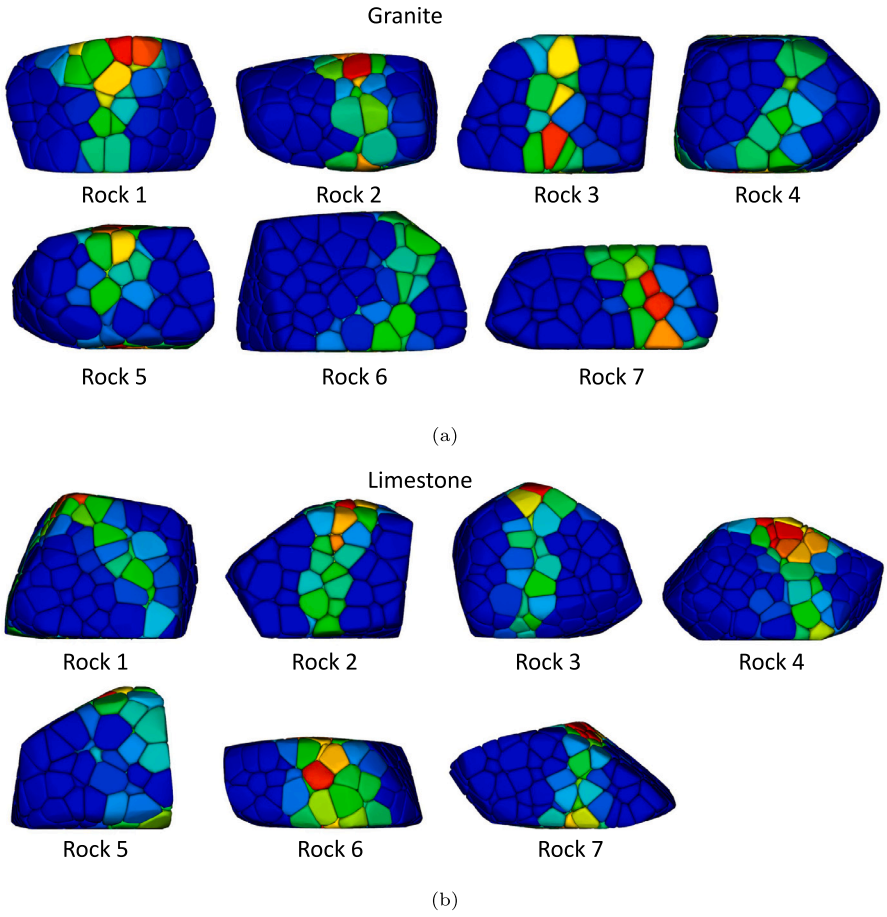

Fig. 13. The damage distribution in the single particle breakage test after fracture is visualized in DEM simulations, where red cells represent that all bonds have failed, and the darkest blue cells indicate that no bonds have failed for (a) granite and (b) limestone. (For interpretation of the references to color in this figure legend, the reader is referred to the web version of this article.)

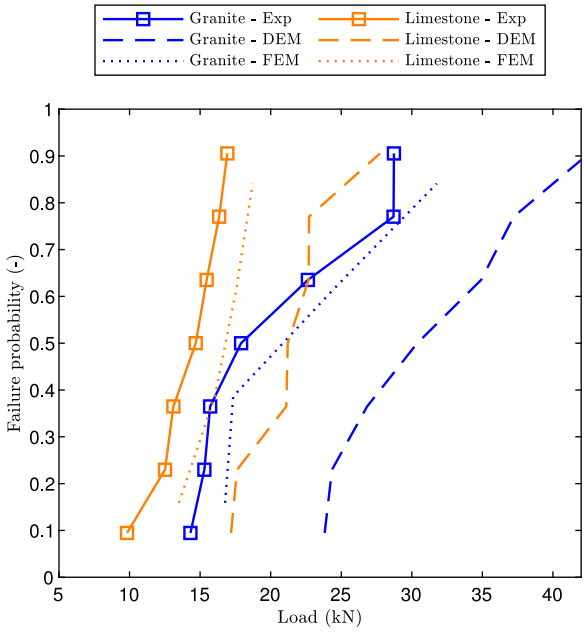

Fig. 14. Cumulative distribution of the failure probability for single particle breakage for experiment, FEM and DEM.

to capture the actual rock material response.

- DEM and FEM validation against single-particle breakage tests with 3D laser-scanned shapes ensured that the rock shapes were known in both the models and experiments. The FEM approach predicted mechanical responses well and provided detailed fracture patterns. The coarser DEM model satisfactorily predicted the overall response, despite mesh coarseness preventing the capture of local contact damage. The lack of local mesh resolution in the contact points leads to a stiffer response than in the FEM model and the experiments, where the material in the contact region is allowed to crumble.
- An industrial-sized cone crusher simulation demonstrated that the bonded DEM models of the rocks can predict all important machine responses at a relevant scale, aligning with the expected values for the chosen crusher machine. Full experimental validation of the cone crusher simulation is omitted for brevity in this work.

In future work, the potential to utilize high-resolution FEM predictions in the further development and calibration of bonded DEM models could be explored. This may complement physical experiments, particularly in advancing predictive capabilities related to mineral lithology and liberation, as the FEM model mesh scale is closer to typical ore mineral grain sizes.

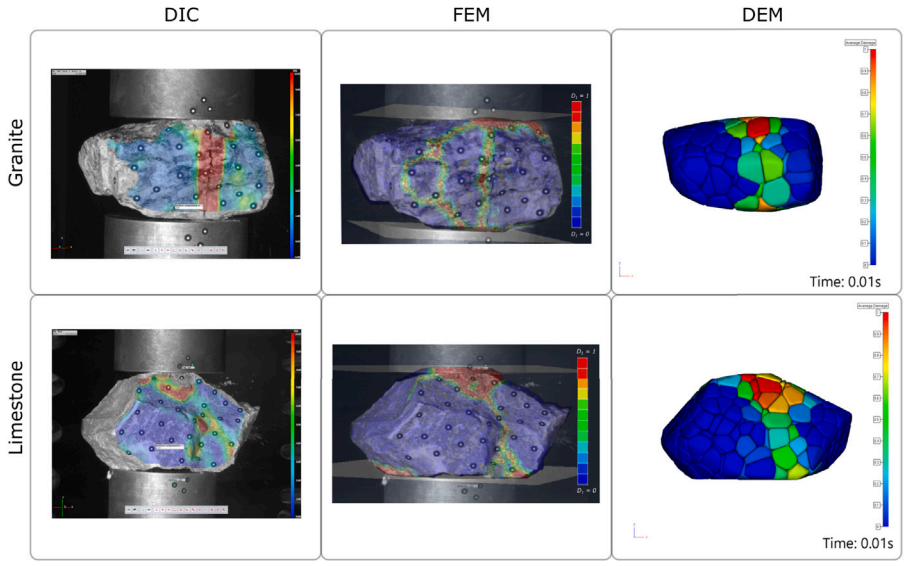

Fig. 15. Comparison of the crack pattern at first fracture for both granite and limestone obtained from DIC, FEM and DEM simulations.

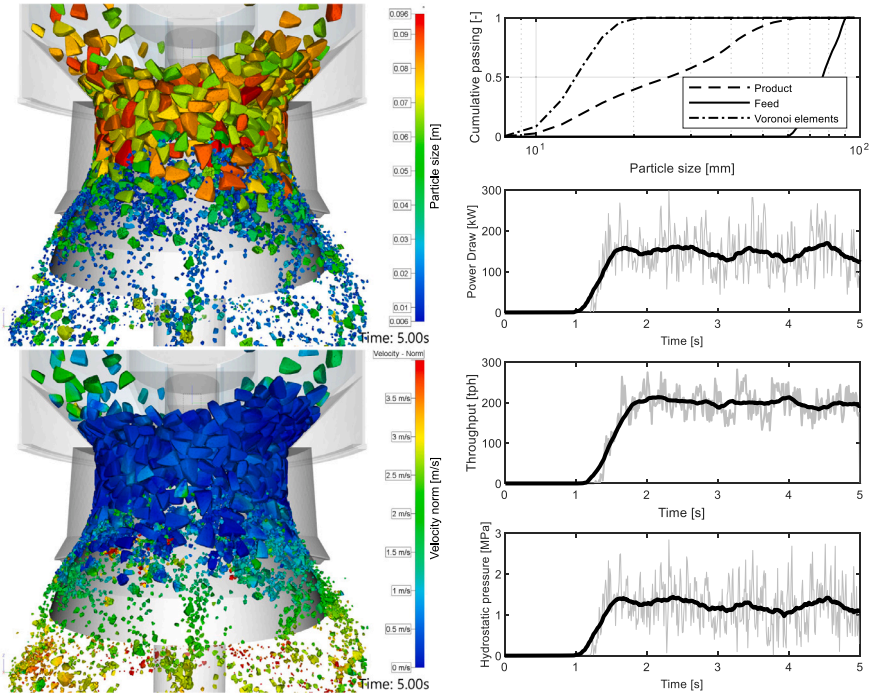

Fig. 16. Compilation of simulation results including simulation snapshot images with particles colored by particle size (top) and velocity (bottom), and size distributions, mass flow throughput, power draw and hydrostatic pressure on the right.

Table 5
Mechanical properties of Brazilian disc specimens. The ultimate tensile strength (UTS) was estimated from Eq. (1).

	ID	Failure load (kN)	UTS (MPa)
Granite	BD-G-01	10.9	11.0
	BD-G-02	15.7	16.2
	BD-G-03	12.3	12.5
	BD-G-04	12.9	13.3
	BD-G-05	13.6	14.0
	BD-G-06	15.8	16.1
	BD-G-07	13.0	13.4
	BD-G-08	11.9	12.0
	BD-G-09	12.0	12.2
	BD-G-10	13.8	13.9
Limestone	BD-L-01	9.8	10.0
	BD-L-02	10.8	11.2
	BD-L-03	10.8	11.1
	BD-L-04	7.9	8.2
	BD-L-05	9.8	10.3
	BD-L-06	9.2	8.8

CRediT authorship contribution statement

Laura Suarez: Writing – review & editing, Writing – original draft, Visualization, Validation, Software, Methodology, Investigation, Formal analysis, Conceptualization. **Vedad Tojaga:** Writing – review & editing, Writing – original draft, Visualization, Software, Methodology, Investigation, Formal analysis, Conceptualization. **Erik Olsson:** Writing – review & editing, Writing – original draft, Supervision, Software, Funding acquisition, Formal analysis. **Adam Bilock:** Writing – review & editing, Software. **Magnus Evertsson:** Writing – review & editing, Resources, Investigation. **Jörgen Kajberg:** Writing – review & editing, Writing – original draft, Supervision. **Johannes Quist:** Writing – review & editing, Writing – original draft, Visualization, Validation, Supervision, Resources, Project administration, Methodology, Investigation, Funding acquisition, Formal analysis, Conceptualization.

Declaration of competing interest

The authors declare that they have no known competing financial interests or personal relationships that could have appeared to influence the work reported in this paper.

Acknowledgments

This work was funded by the ÅForsk Foundation under the project titled Optimization of Crushing in Comminution of Mining Materials – OptiCrush, with the reference number 23-449. The authors also want to thank Prof. Pascal Forquin and Dr. Mahdi Saadati which provided details about implementation of the KST-DFH model.

Appendix

See Tables 5–7.

Data availability

Data will be made available on request.

Table 6
Failure loads from single particle breakage tests of granite and limestone.

	ID	Failure load (kN)
Granite	SPB-G-01	17.9
	SPB-G-02	22.6
	SPB-G-03	15.7
	SPB-G-04	28.7
	SPB-G-05	15.3
	SPB-G-06	28.7
	SPB-G-07	14.3
Limestone	SPB-L-01	16.9
	SPB-L-02	12.5
	SPB-L-03	15.5
	SPB-L-04	16.3
	SPB-L-05	9.8
	SPB-L-06	13.1
	SPB-L-07	14.7

Table 7
DEM meshing parameters used in Demify: pd is an abbreviation for pruning distance.

Brazilian		
50 cells	0.0035 pd	
100 cells	0.003 pd	
150 cells	0.003 pd	
200 cells	0.0025 pd	
250 cells	0.0025 pd	
300 cells	0.0025 pd	
350 cells	0.0025 pd	
400 cells	0.002 pd	
450 cells	0.002 pd	
500 cells	0.002 pd	
SPB granite		
Rock 1	376 cells	0.0035 pd
Rock 2	312 cells	0.0035 pd
Rock 3	206 cells	0.0035 pd
Rock 4	339 cells	0.0035 pd
Rock 5	211 cells	0.0035 pd
Rock 6	372 cells	0.0035 pd
Rock 7	198 cells	0.0035 pd
SPB limestone		
Rock 1	353 cells	0.0035 pd
Rock 2	280 cells	0.0035 pd
Rock 3	381 cells	0.0035 pd
Rock 4	408 cells	0.0035 pd
Rock 5	243 cells	0.0035 pd
Rock 6	349 cells	0.0035 pd
Rock 7	298 cells	0.0035 pd

References

André, F.P., Tavares, L.M., 2020. Simulating a laboratory-scale cone crusher in DEM using polyhedral particles. Powder Technol. 372, http://dx.doi.org/10.1016/j.powtec.2020.06.016.

Aramendia, E., Brockway, P.E., Taylor, P.G., Norman, J., 2023. Global energy consumption of the mineral mining industry: Exploring the historical perspective and future pathways to 2060. Glob. Environ. Chang. 83, 102745. http://dx.doi.org/10.1016/j.gloenvcha.2023.102745.

Asahina, D., Bolander, J., 2011. Voronoi-based discretizations for fracture analysis of particulate materials. Powder Technol. 213 (1), 92–99. http://dx.doi.org/10.1016/j.powtec.2011.07.010.

Barrios, G.K., Jiménez-Herrera, N., Tavares, L.M., 2020. Simulation of particle bed breakage by slow compression and impact using a DEM particle replacement model. Adv. Powder Technol. 31 (7), 2749–2758. http://dx.doi.org/10.1016/j.apt.2020.05.011.

Bažant, Z.P., Tabbara, M.R., Kazemi, M.T., Pijaudier-Cabot, G., 1990. Random particle model for fracture of aggregate or fiber composites. J. Eng. Mech. 116 (8), http://dx.doi.org/10.1061/(asce)0733-9399(1990)116:8(1686).

Benzeggagh, M.L., Kenane, M., 1996. Measurement of mixed-mode delamination fracture toughness of unidirectional glass/epoxy composites with mixed-mode bending apparatus. Compos. Sci. Technol. 56 (4), http://dx.doi.org/10.1016/0266-3538(96)00005-X.

Brzeziński, K., Gladky, A., 2022. Clump breakage algorithm for DEM simulation of crushable aggregates. Tribol. Int. 173, 107661. http://dx.doi.org/10.1016/j.triboint.2022.107661.

Burns, S.J., Piiroinen, P.T., Hanley, K.J., 2019. Critical time step for DEM simulations of dynamic systems using a hertzian contact model. Internat. J. Numer. Methods Engrg. 119 (5), http://dx.doi.org/10.1002/nme.6056.

Cantor, D., Azéma, E., Sornay, P., Radjai, F., 2017. Three-dimensional bonded-cell model for grain fragmentation. Comput. Part. Mech. 4 (4), 441–450. http://dx.doi.org/10.1007/s40571-016-0129-0.

Cleary, P.W., 2001. Recent advances in DEM modelling of tumbling mills. Miner. Eng. 14 (10), http://dx.doi.org/10.1016/S0892-6875(01)00145-5.

Cleary, P.W., Sinnott, M.D., 2015. Simulation of particle flows and breakage in crushers using DEM: Part 1 – compression crushers. Miner. Eng. 74, 178–197. http://dx.doi.org/10.1016/j.mineng.2014.10.021.

Cundall, P., Strack, O., 1979. A discrete numerical model for granular assemblies. Geotechnique 29 (1), 47–65. http://dx.doi.org/10.1680/geot.1979.29.1.47.

Cusatis, G., Pelessone, D., Mencarelli, A., 2011. Lattice discrete particle model (LDPM) for failure behavior of concrete. I: Theory. In: Cement and Concrete Composites. 33, (9), http://dx.doi.org/10.1016/j.cemconcomp.2011.02.011.

de Arruda Tino, A.A., Tavares, L.M., 2022. Simulating breakage tests using the discrete element method with polyhedral particles. Comput. Part. Mech. 9 (4), 811–823. http://dx.doi.org/10.1007/s40571-021-00448-4.

Delaney, G., Morrison, R., Sinnott, M., Cummins, S., Cleary, P., 2015. DEM modelling of non-spherical particle breakage and flow in an industrial scale cone crusher. Miner. Eng. 74, 112–122. http://dx.doi.org/10.1016/j.mineng.2015.01.013.

Denoual, C., Hild, F., 2000. A damage model for the dynamic fragmentation of brittle solids. Comput. Methods Appl. Mech. Engrg. 183 (3), 247–258. http://dx.doi.org/10.1016/S0045-7825(99)00221-2.

Denzel, M., Prenner, M., Sifferlinger, N.A., Antretter, T., 2023. A breakage model for DEM based on a probabilistic particle replacement with voronoi fragments. Miner. Eng. 203, http://dx.doi.org/10.1016/j.mineng.2023.108328.

Dobrilla, S., Lunardelli, M., Nikolić, M., Lowke, D., Rosić, B., 2023a. Bayesian inference of mesoscale mechanical properties of mortar using experimental data from a double shear test. Comput. Methods Appl. Mech. Engrg. 409, http://dx.doi.org/10.1016/j.cma.2023.115964.

Dobrilla, S., Matthies, H.G., Ibrahimbegovic, A., 2023b. Considerations on the identifiability of fracture and bond properties of reinforced concrete. Internat. J. Numer. Methods Engrg. 124 (17), http://dx.doi.org/10.1002/nme.7289.

Eliáš, J., 2014. Simulation of railway ballast using crushable polyhedral particles. Powder Technol. 264, 458–465. http://dx.doi.org/10.1016/j.powtec.2014.05.052.

Ergenzinger, C., Seifried, R., Eberhard, P., 2011. A discrete element model to describe failure of strong rock in uniaxial compression. Granul. Matter 13 (4), http://dx.doi.org/10.1007/s10035-010-0230-7.

Erzar, B., Forquin, P., 2014. Analysis and modelling of the cohesion strength of concrete at high strain-rates. Int. J. Solids Struct. 51 (14), 2559–2574. http://dx.doi.org/10.1016/j.ijsolstr.2014.01.023.

Fairhurst, C., 1964. On the validity of the 'Brazilian' test for brittle materials. Int. J. Rock Mech. Min. Sci. and 1 (4), http://dx.doi.org/10.1016/0148-9062(64)90060-9.

Forquin, P., Hild, F., 2010. A probabilistic damage model of the dynamic fragmentation process in brittle materials. In: Aref, H., van der Giessen, E. (Eds.), Advances in Applied Mechanics. In: Advances in Applied Mechanics, vol. 44, Elsevier, pp. 1–72. http://dx.doi.org/10.1016/S0065-2156(10)44001-6.

François Hild, P.F., da Silva, A.R.C., 2003. Single and multiple fragmentation of brittle geomaterials. Rev. Fran c Caise de Génie Civ. 7 (7–8), 973–1002. http://dx.doi.org/10.1080/12795119.2003.9692529.

Govender, N., Wilke, D.N., Kok, S., Els, R., 2014. Development of a convex polyhedral discrete element simulation framework for NVIDIA Kepler based GPUs. J. Comput. Appl. Math. 270, 386–400. http://dx.doi.org/10.1016/j.cam.2013.12.032, Fourth International Conference on Finite Element Methods in Engineering and Sciences (FEMTEC 2013).

Hondros, G., 1959. The evaluation of Poisson's ratio and the modulus of materials of low tensile resistance by the Brazilian (indirect tensile) test with particular reference to concrete. Aust. J. Appl. Sci. 10 (3), 243–268.

Ibrahimbegovic, A., Delaplace, A., 2003. Microscale and mesoscale discrete models for dynamic fracture of structures built of brittle material. Comput. Struct. 81 (12), http://dx.doi.org/10.1016/S0045-7949(03)00040-3.

Ibrahimbegovic, A., Matthies, H.G., Karavelić, E., 2020. Reduced model of macro-scale stochastic plasticity identification by Bayesian inference: Application to quasi-brittle failure of concrete. Comput. Methods Appl. Mech. Engrg. 372, http://dx.doi.org/10.1016/j.cma.2020.113428.

Jeswiet, J., Szekeres, A., 2016. Energy consumption in mining comminution. Procedia CIRP 48, 140–145. http://dx.doi.org/10.1016/j.procir.2016.03.250, The 23rd CIRP Conference on Life Cycle Engineering.

Jiang, C., Gou, D., Li, C., Wu, G., An, X., Wang, J., Guo, P., 2023. Crushing characteristics and performance evaluation of iron ore in a cone crusher: A numerical study. Miner. Eng. 204, 108429. http://dx.doi.org/10.1016/j.mineng.2023.108429.

Jiménez-Herrera, N., Barrios, G.K., Tavares, L.M., 2018. Comparison of breakage models in DEM in simulating impact on particle beds. Adv. Powder Technol. 29 (3), 692–706. http://dx.doi.org/10.1016/j.apt.2017.12.006.

Jonsén, P., Häggblad, H.Å., Sommer, K., 2007. Tensile strength and fracture energy of pressed metal powder by diametral compression test. Powder Technol. 176 (2–3), 148–155. http://dx.doi.org/10.1016/j.powtec.2007.02.030.

Jou, O., Celigueta, M.A., Latorre, S., Arrufat, F., Oñate, E., 2019. A bonded discrete element method for modeling ship-ice interactions in broken and unbroken sea ice fields. Comput. Part. Mech. 6 (4), http://dx.doi.org/10.1007/s40571-019-00259-8.

Kawamoto, R., Andò, E., Viggiani, G., Andrade, J.E., 2016. Level set discrete element method for three-dimensional computations with triaxial case study. J. Mech. Phys. Solids 91, http://dx.doi.org/10.1016/j.jmps.2016.02.021.

Khanal, M., Schubert, W., Tomas, J., 2005. DEM simulation of diametrical compression test on particle compounds. Granul. Matter 7 (2–3), http://dx.doi.org/10.1007/s10035-005-0200-7.

King, R.P., Bourgeois, F., 1993. Measurement of fracture energy during single-particle fracture. Miner. Eng. 6 (4), http://dx.doi.org/10.1016/0892-6875(93)90015-F.

Krieg, R., 1978. A simple constitutive description for soils and crushable foams. Rep. SC- DR- 7260883, Sandia Natl. Lab..

Kun, F., Herrmann, H.J., 1996. A study of fragmentation processes using a discrete element method. Comput. Methods Appl. Mech. Engrg. 138 (1–4), http://dx.doi.org/10.1016/S0045-7825(96)01012-2.

Li, X., Kuang, J., Jiang, S., Ji, S., 2024. Bonded particle model for dilated polyhedron considering fracture modes and its application to lateral resistance of ballast bed in cold regions. Powder Technol. 439, http://dx.doi.org/10.1016/j.powtec.2024.119673.

Li, H., McDowell, G., Lowndes, I., 2014. Discrete element modelling of a rock cone crusher. Powder Technol. 263, 151–158. http://dx.doi.org/10.1016/j.powtec.2014.05.004.

Liu, L., Ji, S., 2019. Bond and fracture model in dilated polyhedral DEM and its application to simulate breakage of brittle materials. Granul. Matter 21 (3), http://dx.doi.org/10.1007/s10035-019-0896-4.

Liu, G.-Y., Xu, W.-J., Govender, N., Wilke, D.N., 2020. A cohesive fracture model for discrete element method based on polyhedral blocks. Powder Technol. 359, 190–204. http://dx.doi.org/10.1016/j.powtec.2019.09.068.

Ma, Y., Huang, H., 2018. DEM analysis of failure mechanisms in the intact Brazilian test. Int. J. Rock Mech. Min. Sci. 102, http://dx.doi.org/10.1016/j.ijrmms.2017.11.010.

Ma, G., Zhou, W., Chang, X.L., 2014. Modeling the particle breakage of rockfill materials with the cohesive crack model. Comput. Geotech. 61, http://dx.doi.org/10.1016/j.compgeo.2014.05.006.

Ma, G., Zhou, W., Chang, X.-L., Chen, M.-X., 2016. A hybrid approach for modeling of breakable granular materials using combined finite-discrete element method. Granul. Matter 18 (1), 7. http://dx.doi.org/10.1007/s10035-016-0615-3.

Mwanga, A., Rosenkranz, J., Lamberg, P., 2015. Testing of ore comminution behavior in the geometallurgical context-a review. Minerals 5 (2), 276–297. http://dx.doi.org/10.3390/min5020276.

Nikolić, M., Karavelić, E., Ibrahimbegovic, A., Miš˘ cević, P., 2018. Lattice element models and their peculiarities. Arch. Comput. Methods Eng. 25 (3), http://dx.doi.org/10.1007/s11831-017-9210-y.

Nye, B., Kulchitsky, A.V., Johnson, J.B., 2014. Intersecting dilated convex polyhedra method for modeling complex particles in discrete element method. Int. J. Numer. Anal. Methods Geomech. 38 (9), http://dx.doi.org/10.1002/nag.2299.

Olsson, E., Jelagin, D., Forquin, P.A., 2019. Computational framework for analysis of contact-induced damage in brittle rocks. Int. J. Solids Struct. 167, 24–35. http://dx.doi.org/10.1016/j.ijsolstr.2019.03.001.

Orozco, L.F., Delenne, J.-Y., Sornay, P., Radjai, F., 2019. Discrete-element model for dynamic fracture of a single particle. Int. J. Solids Struct. 166, 47–56. http://dx.doi.org/10.1016/j.ijsolstr.2019.01.033.

Potapov, A.V., Campbell, C.S., 1994. Computer simulation of impact-induced particle breakage. Powder Technol. 81 (3), http://dx.doi.org/10.1016/0032-5910(94)02907-5.

Potyondy, D.O., Cundall, P.A., 2004. A bonded-particle model for rock. Int. J. Rock Mech. Min. Sci. 41 (8 SPEC.ISS.), http://dx.doi.org/10.1016/j.ijrmms.2004.09.011.

Quist, J., Evertsson, C.M., 2016. Cone crusher modelling and simulation using DEM. Miner. Eng. 85, 92–105. http://dx.doi.org/10.1016/j.mineng.2015.11.004.

Rozmanov, D., Kusalik, P.G., 2010. Robust rotational-velocity-verlet integration methods. Phys. Rev. E - Stat. Nonlinear, Soft Matter Phys. 81 (5), http://dx.doi.org/10.1103/PhysRevE.81.056706.

Rycroft, C.H., 2009. VORO++: A three-dimensional voronoi cell library in C++. Chaos 19 (4), http://dx.doi.org/10.1063/1.3215722.

Saadati, M., Forquin, P., Weddfelt, K., Larsson, P.-L., 2016. On the tensile strength of granite at high strain rates considering the influence from preexisting cracks. Adv. Mater. Sci. Eng. 2016, 1–9. http://dx.doi.org/10.1155/2016/6279571.

Saadati, M., Forquin, P., Weddfelt, K., Larsson, P., Hild, F., 2014. Granite rock fragmentation at percussive drilling-experimental and numerical investigation. Int. J. Numer. Anal. Methods Geomech. 38 (8), 828–843. http://dx.doi.org/10.1002/nag.2235.

Saadati, M., Forquin, P., Weddfelt, K., Larsson, P.L., Hild, F., 2018. On the mechanical behavior of granite material with particular emphasis on the influence from pre-existing cracks and defects. J. Test. Eval. 46 (1), 33–45. http://dx.doi.org/10.1520/JTE20160072.

Saksala, T., 2010. Damage–viscoplastic consistency model with a parabolic cap for rocks with brittle and ductile behavior under low-velocity impact loading. Int. J. Numer. Anal. Methods Geomech. 34 (13), 1362–1386. http://dx.doi.org/10.1002/nag.868.

Saksala, T., Hokka, M., Kuokkala, V.-T., Mäkinen, J., 2013. Numerical modeling and experimentation of dynamic Brazilian disc test on kuru granite. Int. J. Rock Mech. Min. Sci. 59, 128–138. http://dx.doi.org/10.1016/j.ijrmms.2012.12.018.

Swenson, D.V., Taylor, L.M., 1983. A finite element model for the analysis of tailored pulse stimulation of boreholes. Int. J. Numer. Anal. Methods Geomech. 7 (4), 469–484. http://dx.doi.org/10.1002/nag.1610070408.

Tavares, L.M., 2007. Chapter 1 breakage of single particles: Quasi-static. In: Salman, A.D., Ghadiri, M., Hounslow, M.J. (Eds.), Particle Breakage. In: Handbook of Powder Technology, vol. 12, Elsevier Science B.V., pp. 3–68. http://dx.doi.org/10.1016/S0167-3785(07)12004-2.

Tavares, L.M., André, F.P., Potapov, A., Maliska, C., 2020. Adapting a breakage model to discrete elements using polyhedral particles. Powder Technol. 362, 208–220. http://dx.doi.org/10.1016/j.powtec.2019.12.007.

Tavares, L.M., King, R.P., 1998. Single-particle fracture under impact loading. Int. J. Miner. Process. 54 (1), http://dx.doi.org/10.1016/s0301-7516(98)00005-2.

Tavares, L.M., King, R.P., 2002. Modeling of particle fracture by repeated impacts using continuum damage mechanics. Powder Technol. 123 (2–3), http://dx.doi.org/10.1016/S0032-5910(01)00438-7.

Tavares, L.M., Rodriguez, V.A., Sousani, M., Padros, C.B., Ooi, J.Y., 2021. An effective sphere-based model for breakage simulation in DEM. Powder Technol. 392, 473–488. http://dx.doi.org/10.1016/j.powtec.2021.07.031.

Unland, G., 2007. Chapter 4 the principles of single-particle crushing. In: Handbook of Powder Technology. 12, (ISSN: 01673785) http://dx.doi.org/10.1016/S0167-3785(07)12007-8.

Wang, T., Liu, H.Z., Xiao, M.L., Zhuo, L., Xie, H.Q., He, J.D., 2023. Improvement of size effect simulation based on an energy-balanced exponential softening bond model and fracture energy regularization. Comput. Struct. 280, http://dx.doi.org/10.1016/j.compstruc.2023.107004.

Weerasekara, N., Powell, M., Cleary, P., Tavares, L., Evertsson, M., Morrison, R., Quist, J., Carvalho, R., 2013. The contribution of DEM to the science of comminution. Powder Technol. 248, 3–24. http://dx.doi.org/10.1016/j.powtec.2013.05.032.

Wessling, A., Larsson, S., Jonsén, P., Kajberg, J., 2022. A statistical DEM approach for modelling heterogeneous brittle materials. Comput. Part. Mech. 9 (4), http://dx.doi.org/10.1007/s40571-021-00434-w.

Wessling, A., Larsson, S., Kajberg, J., 2023. A statistical bonded particle model study on the effects of rock heterogeneity and cement strength on dynamic rock fracture. Comput. Part. Mech. http://dx.doi.org/10.1007/s40571-023-00688-6.

Yoon, J., 2007. Application of experimental design and optimization to PFC model calibration in uniaxial compression simulation. Int. J. Rock Mech. Min. Sci. 44 (6), http://dx.doi.org/10.1016/j.ijrmms.2007.01.004.

Yuan, R., Shen, B., 2017. Numerical modelling of the contact condition of a Brazilian disk test and its influence on the tensile strength of rock. Int. J. Rock Mech. Min. Sci. 93, 54–65. http://dx.doi.org/10.1016/j.ijrmms.2017.01.010.

Zhao, J., Zhao, S., Luding, S., 2023. The role of particle shape in computational modelling of granular matter. In: Nature Reviews Physics. 5, (9), (ISSN: 25225820) http://dx.doi.org/10.1038/s42254-023-00617-9.

Zubelewicz, A., Bažant, Z.P., 1987. Interface element modeling of fracture in aggregate composites. J. Eng. Mech. 113 (11), 1619–1630.